

The environments of Ly α blobs I: Wide-field Ly α imaging of TN J1338-1942, a powerful radio galaxy at $z \simeq 4.1$ associated with a giant Ly α nebula ^{*}

Tomoki Saito^{1†}, Yuichi Matsuda^{2,3}, Cedric G. Lacey⁴, Ian Smail⁴, Alvaro Orsi^{5,6}, Carlton M. Baugh⁴, Akio K. Inoue⁷, Ichi Tanaka⁸, Toru Yamada⁹, Kouji Ohta¹⁰, Carlos De Breuck¹¹, Tadayuki Kodama^{2,3}, Yoshiaki Taniguchi¹²

¹*Kavli Institute for the Physics and Mathematics of the Universe (WPI), Todai Institutes for Advanced Studies, The University of Tokyo, 5-1-5 Kashiwanoha, Kashiwa, Chiba 277-8583, Japan*

²*National Astronomical Observatory of Japan, 2-21-1 Osawa, Mitaka, Tokyo 181-8588, Japan*

³*The Graduate University for Advanced Studies (SOKENDAI), 2-21-1 Osawa, Mitaka, Tokyo 181-0015, Japan*

⁴*Institute for Computational Cosmology, Department of Physics, Durham University, South Road, Durham DH1 3LE, UK*

⁵*Instituto de Astrofísica, Facultad de Física, Pontificia Universidad Católica, Av. Vicuña Mackenna 4860, Santiago, Chile*

⁶*Centro de Astro-Ingeniería, Pontificia Universidad Católica, Av. Vicuña Mackenna 4860, Santiago, Chile*

⁷*College of General Education, Osaka Sangyo University, 3-1-1, Nakagaito, Daito, Osaka 574-8530, Japan*

⁸*Subaru Telescope, National Astronomical Observatory of Japan, 650 North A'ohoku Place, Hilo, HI 96720, USA*

⁹*Astronomical Institute, Tohoku University, Aramaki, Aoba, Sendai 980-8578, Japan*

¹⁰*Department of Astronomy, Kyoto University, Kyoto 606-8502, Japan*

¹¹*European Southern Observatory, Karl Schwarzschild Straße 2, 85748 Garching, Germany*

¹²*Research Center for the Space and Cosmic Evolution, Ehime University, 2-5 Bunkyo-cho, Matsuyama, Ehime 790-8577, Japan*

Draft version 20 Mar. 2014

ABSTRACT

We present wide-field Ly α imaging observations of the field around TN J1338–1942, a powerful radio galaxy associated with an extended Ly α nebula (> 100 kpc) at $z = 4.11$, with Subaru Prime-focus Camera to probe the environment of the radio galaxy. We used a sample of Ly α emitters (LAEs) down to the Ly α luminosity of $\log(L_{\text{Ly}\alpha}[\text{erg s}^{-1}]) \sim 42.8$ to measure the galaxy density of this field, calibrating by direct comparison with a control sample in a blank field taken with the same instrument. We found that the radio galaxy resides in a region with a peak overdensity of $\delta_{\text{LAE}} = 3.1 \pm 0.5$, after being smoothed on $8 h^{-1} \text{Mpc}$ scales on the sky and $160 h^{-1} \text{Mpc}$ along the line of sight (both in comoving coordinates). Adjacent to this overdense region, we found a highly underdense region where virtually no LAEs are detected. We used a semi-analytical model of LAEs derived from the Millennium Simulation to compare our results with theoretical predictions. This comparison suggests that, while the density distribution of the simulation is consistent with that of the blank field, overdense regions such as the one found in the radio galaxy field are very rare, with the number density of $2 \times 10^{-7} h^3 \text{Mpc}^{-3}$ (comoving), corresponding to the densest < 0.1 percentile at these redshifts. We also found a difference in the Ly α luminosity function in the radio galaxy field compared with the blank field: the number of bright LAEs ($\log(L_{\text{Ly}\alpha}[\text{erg s}^{-1}]) \gtrsim 43.3$) is enhanced, while the number of fainter LAEs is relatively suppressed. These results suggest that some powerful radio galaxies associated with Ly α nebulae reside in extreme overdensities on $\sim 10\text{--}20 h^{-1} \text{Mpc}$ scales, where star-formation and AGN activities may be enhanced via more frequent galaxy mergers or higher rates of gas accretion from the surroundings.

Key words: galaxies: evolution – galaxies: formation – galaxies: high-redshift – galaxies: individual: TN J1338–1942

^{*} Based on data collected at Subaru Telescope, which is operated by the National Astronomical Observatory of Japan.

[†] E-mail: tomoki.saito@ipmu.jp (TS),
yuichi.matsuda@nao.ac.jp (YM)

1 INTRODUCTION

Galaxies are thought to form through accretion of baryonic material (Pre-Galactic Medium, PGM) from their surrounding environment, which provides the cold gas necessary for the star-formation process to proceed. The classical picture of this accretion is that the PGM is immediately heated to the virial temperature of the dark haloes (typically $\sim 10^6$ K) to form hot haloes (e.g. Rees & Ostriker 1977). Recent theoretical studies, in contrast, predict that cold gas accretes in the form of cold flows (with temperatures of $\lesssim 10^5$ K) which penetrate the hot haloes surrounding the galaxies and which over cosmic time maintain the star-formation activity in galaxies (e.g. Kereš et al. 2005; Dekel et al. 2009). At these low temperatures the gas in the PGM will predominantly cool via Ly α emission. The star-formation episodes powered by this accretion in turn provide a stellar feedback mechanisms which can then re-heat and eject material in the form of galactic-scale outflows (galactic winds: e.g. Veilleux et al. 2005; Steidel et al. 2010), which subsequently interact with the ambient material in the Circum-Galactic Medium (CGM). Hence both the accretion and outflows mean that galaxies interact with their surrounding environments, potentially resulting in extended Ly α emission either through cold accretion of the PGM (e.g. Fardal et al. 2001; Dijkstra et al. 2006; Dijkstra & Loeb 2009; Faucher-Giguère et al. 2010; Goerdt et al. 2010), or from galactic winds ejected into CGM (e.g. Tenorio-Tagle et al. 1999; Taniguchi & Shioya 2000; Mori & Umemura 2006; Dijkstra & Kramer 2012). Such Ly α nebulae may therefore reflect either the structure of the surrounding material, or gas circulation processes during the formation/evolution of these galaxies (Furlanetto et al. 2005).

The precise mechanisms responsible for forming Ly α nebulae are still unclear. Some Ly α nebulae (e.g., those in the SA 22 protocluster at $z = 3.1$) have been extensively observed, and are thought to be driven by starburst events in massive galaxies forming galactic winds (e.g. Ohya et al. 2003; Wilman et al. 2005; Matsuda et al. 2006; Geach et al. 2005; Geach et al. 2009; Uchimoto et al. 2008, 2012). Moreover, recent surveys targeting Ly α “blobs” have also suggested a possible connection between their properties (specifically morphologies) and the environments they reside in (Erb et al. 2011; Matsuda et al. 2011, 2012). Such an environmental dependence is also qualitatively consistent with the observations of relatively isolated Ly α nebulae, which may point to the possibility that these are accretion-driven (Nilsson et al. 2006; Smith & Jarvis 2007; Saito et al. 2008). However, to determine the true significance of environment in the formation of extended Ly α emission haloes, more detailed and systematic observations with sufficient depth and area are essential.

It has been long known that powerful radio galaxies at high redshifts are often associated with large, extended Ly α nebulae (e.g. Chambers et al. 1990; Röttgering et al. 1995; van Ojik et al. 1996, 1997; Venemans et al. 2007; Villar-Martin et al. 2007). Although these Ly α nebulae appear linked to the radio emission, their properties are similar to the Ly α blobs described above. For example, the large velocity widths exceeding $\sim 1000 \text{ km s}^{-1}$ (van Ojik et al. 1997) or absorption across the full extent of the Ly α nebulae (Röttgering et al. 1995; van Ojik et al. 1996) are also

seen in the Ly α nebulae in protoclusters (e.g. Wilman et al. 2005; Matsuda et al. 2006). There appears to be a size dependence of the Ly α nebulae on the size of radio sources (van Ojik et al. 1997), as well as a hint of environmental dependence on the size of the Ly α nebulae (Venemans et al. 2007). Even for those Ly α blobs not directly associated with radio sources, these are sometimes found to be harbouring AGNs (e.g. Basu-Zych & Scharf 2004; Geach et al. 2009). These results suggest that Ly α nebulae are common phenomena reflecting the interaction between massive galaxies and their surrounding environments, regardless of the presence of AGNs. It is thus quite essential to probe the environments of Ly α nebulae with and without radio sources.

We have conducted a systematic, wide-field imaging observations of the environments around known giant Ly α nebulae, as traced by Ly α emitters (LAEs). Here we present the results from the imaging of the first target, the powerful radio galaxy TN J1338–1942 (hereafter TNJ1338) located at $z = 4.11$ (De Breuck et al. 1999). This radio galaxy is known to have a Ly α nebula extending up to ~ 100 kpc with an asymmetric morphology (Venemans et al. 2002). It has been suggested that this source is associated with a highly overdense region traced by LAEs and Lyman break galaxies, and thus represents an ancestor of present-day clusters, i.e., a *protocluster* (Miley et al. 2004; Venemans et al. 2002, 2007; Intema et al. 2006; Overzier et al. 2008). Theoretical simulations also suggests that the overdensity associated with TNJ1338 is likely to be an ancestor of a present-day cluster (Chiang et al. 2013). Multiwavelength observations have shown that this source has radio lobes with an extent of ~ 70 kpc. (De Breuck et al. 2004; Venemans et al. 2007). The extended Ly α nebula around this source has signatures of star-formation induced by the radio jet, well outside the host galaxy at radii of ~ 20 kpc or more (Zirm et al. 2005). Finally, *Chandra* X-ray observations indicate that there is weak extended emission (~ 30 kpc) which may arise from inverse-compton scattering of cosmic microwave background or locally-produced far-infrared photons (Smail & Blundell 2013).

Together these observations suggest a number of processes responsible for intense interaction between the central radio galaxy and the surrounding environment. However, due to the lack of the wide-field imaging data, the surrounding environment of this radio galaxy is still not well characterised. The existing LAE survey data cover a small field (two $7' \times 7'$) making it hard to map any overdensity, and there is no matched blank field observations which means that even the magnitude of the overdensity is uncertain. (Venemans et al. (2007) used the Large-Area Lyman Alpha (LALA) survey results (Rhoads et al. 2000; Dawson et al. 2004) for the reference, which are taken with the different telescope and instrument, targeting a slightly different redshift). Accordingly the relationship between the structure hosting the radio galaxy (and the protocluster) and the wider surrounding environment cannot be probed with the existing data.

The goal of our study is to better quantify the environment of the powerful radio galaxy TNJ1338. To this end we have obtained wide-field intermediate-band images to identify the LAEs lying at the redshift of the radio galaxy, and so quantify the environment using the LAE number density. The magnitude of the overdensity was determined from

Table 1. Summary of Observations

Filter	$\lambda_{\text{cent}}/\Delta\lambda$ ^a [Å/Å]	Exposure Time [sec]	$m_{5\sigma}$ ^b [AB mag]	PSF ^c [″]
<i>IA624</i>	6226/302	28800 (1800 × 16)	26.94	0.74
<i>B</i>	4417/807	4800 (1200 × 4)	26.87	0.80
<i>R</i>	6533/1120	5940 (540 × 11)	26.92	0.55
<i>BR</i> ^d	6226/1927	–	26.90	0.74

^aThe central wavelength and FWHM of the filters.

^bThe 5σ limiting magnitudes within a $1.5''$ diameter aperture.

^cThe median PSF size (FWHM).

^dThe weighted mean of the *B* and *R*-band images.

comparison with a control sample taken from a blank field, SXDS (Furusawa et al. 2008), at the same redshift and with the same instrumental setup (Saito et al. 2006). This enables us to probe “*on what scale does a significant overdensity exist?*”, i.e., the amplitude of the overdensity and the spatial extent of the protocluster. We also compare our observations with predictions derived from combining the Millennium Simulation (Springel et al. 2005) with a semi-analytical model for LAEs (Orsi et al. 2008). This allows us to estimate how rare is the overdensity found around the radio galaxy, and more generally how well the simulation can reproduce such environments. This is the first truly panoramic ($\sim 30' \times 30'$) systematic and quantitative study of the environment of a radio galaxy field at $z \sim 4$.

The rest of this paper is organized as follows: We introduce the data and observational details in §2. The procedure to select LAEs from these data are presented in §3. In §4, we compare the observed density field and luminosity function of LAEs in the radio galaxy field and the blank field, and then compare the observations to the mock LAEs from the theoretical simulations. Throughout this paper, we use the standard Λ CDM cosmology with $\Omega_M = 0.3, \Omega_\Lambda = 0.7$, $H_0 = 100h = 70\text{km s}^{-1}\text{Mpc}^{-1}$, unless otherwise noted. All the magnitudes are in AB system (Oke 1974; Fukugita et al. 1995).

2 THE DATA

2.1 Subaru imaging data

We obtained 8.0 hours integration through the *IA624* intermediate-band filter centred at $(\alpha, \delta) = (13^{\text{h}}38^{\text{m}}13.9^{\text{s}}, -19^{\circ}42'29'')$ (J2000.0) on 2008 May 31 and June 01 (UT) with Suprime-Cam (Miyazaki et al. 2002) on the 8.2-m Subaru Telescope (Iye et al. 2004), under the proposal ID S08A-072 (PI: Y. Matsuda). For the continuum correction we obtained archival broad-band imaging in the *B* and *R*-bands taken by Intema et al. (2006) from the archive system SMOKA (Baba et al. 2002). Details of the observations are summarized in Table 1. Suprime-Cam has a pixel scale of $0''.202$ and a field of view of $34' \times 27'$. The intermediate-band filter, *IA624*, has a central wavelength of 6226Å and bandwidth of 302Å (FWHM), which corresponds to the redshift range for Ly α at $z = 3.996\text{--}4.245$ (*R23 IA filter system*: Hayashino et al. 2000; Taniguchi 2004). Fig. 1 shows the transmission curves of the *IA624*, *B* and

R-band filters, and the observed-frame wavelength of the Ly α line at the redshift of TNJ1338 ($z = 4.11$).

The raw data were reduced with SDFRED20080620 (Yagi et al. 2002; Ouchi et al. 2004) and IRAF. We flat-fielded using the median sky image after masking sources. We then subtracted the sky background adopting a mesh size of 64 pixels ($13''$) before combining the images. Photometric calibration was obtained from the spectroscopic standard stars, PG1323–086, and PG1708+602 (Massey et al. 1988; Stone 1996). The magnitudes were corrected for Galactic extinction of $E(B-V) = 0.10$ mag (Schlegel, Finkbeiner, & Davis 1998). The variation of the extinction in this field is sufficiently small (± 0.01 mag from peak to peak) that it does not affect our results.

The combined images were aligned and smoothed with Gaussian kernels to match their PSF to a FWHM of $0''.74$. The PSF sizes for some exposures in the *B* band were not as good as the other bands (the median PSF size was $0.8''$), so that we removed these bad-seeing data, using only the four best frames for our analysis. The total size of the field analysed here is $32' \times 24'$ after the removal of low-S/N regions near the edges of the images. We also masked out the haloes of the bright stars within the field, resulting in the effective area of 689 arcmin² in total. This corresponds to a comoving volume of $1.7 \times 10^5 h^{-3} \text{Mpc}^3$ at $z = 4.1$, covering a radial comoving distance of $160.5 h^{-1} \text{Mpc}$ for sources with Ly α emission lying within the wavelength coverage of the *IA624* filter.

The blank-field data used for the control sample were taken as part of the Subaru/*XMM-Newton* Deep Survey (SXDS) project (Furusawa et al. 2008) and a subsequent intermediate-band survey (Saito et al. 2006). The SXDS field consists of five pointings, centred at $(\alpha, \delta) = (02^{\text{h}}18^{\text{m}}00.0^{\text{s}}, -5^{\circ}00'00.0'')$ (J2000). The intermediate-band (including *IA624*) data were taken only in the south field (SXDS-S) centred at $(\alpha, \delta) = (02^{\text{h}}18^{\text{m}}00.0^{\text{s}}, -5^{\circ}25'00.0'')$ (J2000). The data were taken with the same instrument on the same telescope, and reduced in the same manner with the same software as our TNJ1338 observations. The PSF was matched to $0''.78$ (FWHM), and the 5σ limiting magnitudes are 26.60, 27.42 and 27.91 for the *IA624*, *B* and *R*, respectively. After masking out the regions near the edges and bright stars, the total area coverage was 691 arcmin², which is almost the same as the TNJ1338 field.

2.2 Mock catalogue of Ly α emitters

In order to compare the observations with the predictions from a cosmological *N*-body simulation (Millennium Simulation: Springel et al. 2005), we exploited a LAE catalogue generated with a semi-analytical model of galaxy formation (GALFORM Cole et al. 2000; Le Delliou et al. 2005, 2006). This catalogue contains $\sim 10^6$ LAEs with a wide range of luminosity and the Ly α equivalent widths (EWs). The details of this catalogue are described in Orsi et al. (2008). The LAEs in this catalogue were generated by placing model galaxies into dark haloes of masses above the threshold value appropriate for the simulation’s mass resolution. The star-formation history for each halo was calculated by using a Monte-Carlo merger tree. The IMF was assumed to be top heavy for those stars formed during any

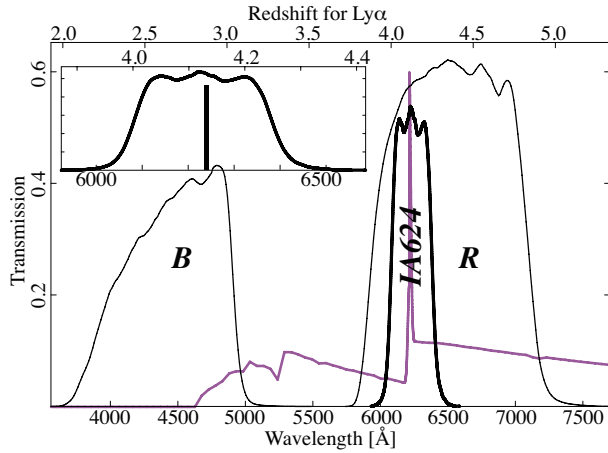


Figure 1. The response curves of our filters. The transmission of the filters are plotted against the wavelength. The lower axis shows the observed wavelength, and the upper axis gives the corresponding redshift for Ly α line. The thick black curve shows the intermediate-band filter (*IA624*) used to select sources with Ly α emission. The two broadband filters (*B* and *R*) are shown with thin lines. The thick magenta curve shows a model SED of a star-forming galaxy created with *GALAXEV* (Bruzual & Charlot 2003) with a Gaussian-profile Ly α emission line, redshifted to $z = 4.1$. The box in the upper-left shows a close-up view of the *IA624* filter transmission, together with the redshift of TNJ1338 indicated with a vertical thick bar.

starbursts, $dN/d\ln(m) \propto m^{-x}$ with $x = 0$, with a standard solar neighbourhood IMF (Kennicutt 1983) for those stars which quiescently form in discs, i.e. $x = 0.4$ for $m < 1M_{\odot}$ and $x = 1.5$ for $m > 1M_{\odot}$. Both IMFs covers the stellar-mass range $0.15M_{\odot} < m < 125M_{\odot}$. The Ly α line luminosity is then calculated from the number of ionising photons emitted by the corresponding stellar population.

Orsi et al. (2008) compared the properties of model LAEs from their simulation with existing LAE surveys and showed that both the luminosity function (LF) and the clustering properties are broadly consistent with the observations. The number density of model LAEs in the luminosity range of $\sim 10^{42.5} - 10^{43} \text{ erg s}^{-1}$ are slightly higher than observed in the SXDS at $z = 3.1$, but slightly below the SXDS at $z = 5.7$. The difference is up to $\sim 0.5 \text{ dex}$, so that the accuracy of the model prediction for the LFs should be around $\sim \pm 0.5 \text{ dex}$. From this catalogue we selected LAEs using similar colour constraints to those applied to the observed data, see §3 for details of the selection procedure.

3 SAMPLE SELECTION

3.1 The TNJ1338 field sample

We used the *IA624* image for detection, and the wavelength-weighted mean of *B* and *R* band images (hereafter *BR*) to determine the continuum level at a rest-frame wavelength of 1216\AA . The *BR* image was generated by combining the two images with:

$$BR = \frac{(\lambda_{Ly\alpha,obs} - \lambda_B)R + (\lambda_R - \lambda_{Ly\alpha,obs})B}{\lambda_R - \lambda_B}$$

where λ_B and λ_R are the central wavelengths of *B* and *R* bands, respectively, and the $\lambda_{Ly\alpha,obs}$ is the observed-frame wavelength of the Ly α line at $z = 4.11$. The source detection and photometry were made using the source- detection and classification tool, SExtractor (Bertin & Arnouts 1996). The sources detected here have at least five connected pixels above a threshold corresponding to 1.5σ of the sky noise. Using the position of these sources detected in the *IA624* image, photometry was measured in the other bands with the same aperture, after matching the PSF size. We measured photometry for a total of 205,011 sources, after masking.

Based on the photometry catalogue from these three images (*B*, *R*, and *IA624*), we selected the LAE candidates at $z \simeq 4.1$ by applying the following conditions.

$$20 < IA624 < 26.6 \quad (1)$$

$$BR - IA624 > 0.3 \quad (2)$$

$$B > 27.87, \text{ or } B - R > 2.17 \quad (3)$$

$$BR - IA624 > (BR - IA624)_{4\sigma} \quad (4)$$

We first applied the magnitude cut (eq. 1) to remove bright foreground contaminants ($IA624 > 20$) and a faint limit to remove false detections ($IA624 > 5\sigma$). Note that the 5σ threshold here is set according to the SXDS data, not the TNJ1338 data, in order to make a fair comparison with the control sample obtained in the SXDS field. The bright threshold, 20 mag, was determined from visual inspection of the sources. This value roughly corresponds to Ly α luminosities corresponding to the brightest high-redshift radio galaxies (e.g., De Breuck et al. 2001; Reuland et al. 2003). Eq. 2 selects those sources with Ly α excess in the intermediate band filter, corresponding to an equivalent width of $\gtrsim 200\text{\AA}$ ($\gtrsim 40\text{\AA}$ in the rest frame). Then we applied a colour selection designed to detect the Lyman-break at $z \sim 4$ (eq. 3). Finally, eq. 4 requires that the *IA624* excess has a significance level of at least 4σ . Note that we used the *BR* matched-continuum to estimate the *IA624* excess, although the *B* band should detect almost no flux from $z \sim 4$ sources because the wavelength coverage of the *B* band is mostly below the Lyman limit. However, the distribution of the *R* – *IA624* colour is not centred at zero, so that defining *IA624*-excess sources using just the *R*-band continuum level is somewhat unclear. We thus used the *BR* to measure the continuum levels.

Fig. 2 shows the colour-magnitude diagram used for our LAE selection. We need to be aware of the possible contamination due to the noise in the *IA624* excess measurements: the LAEs should lie well above the scatter around $BR - IA624 = 0$. For some cases, i.e., when the *IA624* is relatively shallow, false detections may dominate sources selected at the 3σ level. We carefully visual inspected all the sources selected here, and we found one source that is obviously affected by bad regions of the CCD. This source is in a region affected by a neighbouring bright source. Excluding this, we constructed a sample of 32 LAEs in the TNJ1338 field.

Fig. 3 shows the sky distribution of the LAEs selected above, overlaid on the *IA624* image. The reader should note the apparent “void” around the north-western part of the field, where relatively few LAEs are detected, and does not seem to be an artifact of the bright stars.

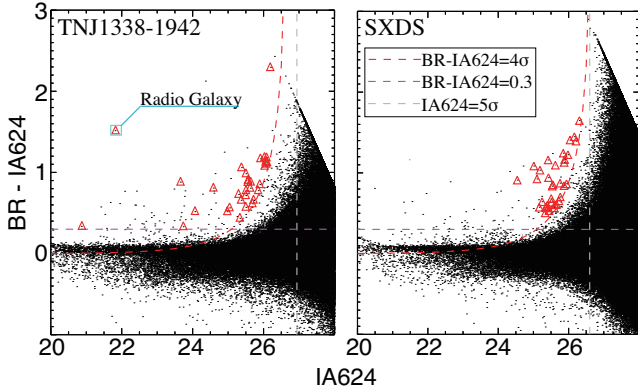


Figure 2. Colour-magnitude diagram. $BR - IA624$ colour as a function of $IA624$ magnitude for the TNJ1338 field. (Left) The black dots show all the sources, and the red triangles show 4σ -excess LAE candidates. The vertical grey dashed line shows the magnitude cut ($IA624 > 26.6$), the horizontal magenta dashed line indicates the $BR - IA624 > 0.3$ threshold. The red dashed curves show 4σ level of the $IA624$ excess. (Right) Same as the left panel, but for the SXDS blank field.

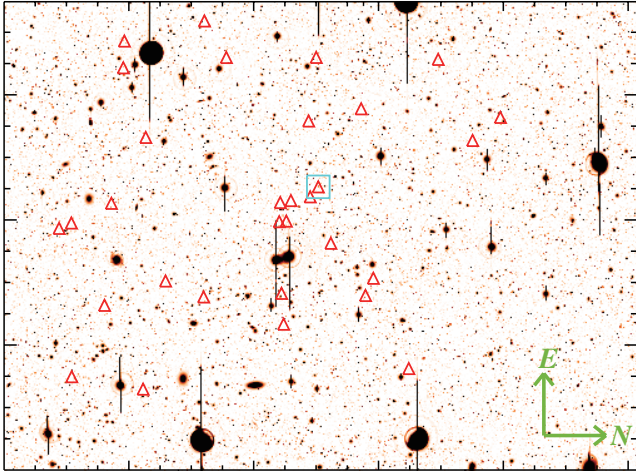


Figure 3. The sky distribution of our LAEs in the TNJ1338 field. The symbols for our photometrically-selected LAE sample are the same as Fig. 2, and the position of TNJ1338 is shown with the cyan box. The background is the $IA624$ image taken with Suprime-Cam. East is up, and north is to the right

3.2 The control sample in SXDS field

We constructed a control sample of LAEs, using similar imaging data in a blank field (the SXDS-S field, hereafter SXDS). These data were taken with the same instrument and filters as used in the TNJ1338 observations as noted above, and the field is not biased to any known overdense regions at $z \sim 4$. In order to make a fair comparison between the two fields, we defined the colour constraints based on the shallower data of the two, i.e., 5σ limiting magnitudes are assumed to be $IA624 = 26.60$ mag, $R = 26.94$ mag, and $B = 26.87$ mag. We also corrected for the offset of $BR - IA624$ colour distribution for the SXDS field, presumably due to an error in the magnitude zero point. We then applied a colour term $\Delta(BR - IA624) = 0.15$. This colour term was estimated by fitting a Gaussian function to the

colour distribution. We derived the colour offset necessary to force the centre of the colour distribution to zero within the magnitude range $20 < IA624 < 26.60$. Except for applying this colour term, we employed exactly the same colour constraints to select the LAEs in this field. The total number of sources identified is 34. The colour-magnitude diagram for this sample is shown in Fig. 2 together with the TNJ1338 sample.

3.3 The mock LAE sample

In order to make a meaningful comparison between the observations and the simulation, we selected LAEs from the mock LAE catalogue at $z = 4.17$ described in §2, which is the output redshift closest to that of TNJ1338. We used the predicted Ly α fluxes and EWs contained in the catalogue, to calculate the colours and magnitudes of the LAEs. Note that the catalogue contains $z = 4.17$ LAEs, while we are going to constrain the observed (apparent) colours of $z \approx 4.11 \pm 0.12$. However, the difference between these two epochs is very small, ~ 55 Myr, and $z = 4.17$ is well within the coverage of the $IA624$ filter. We thus calculated the apparent (observed) colours at $z = 4.11$. This should be a reasonable assumption to compare the simulated LAEs with the observations, since the timescale of galaxy evolution (e.g., star formation) is much longer than this difference.

We first calculated the absorption of the UV continuum by the intervening IGM, following the formalism of Madau (1995). Here the UV continuum was assumed to be flat in terms of flux density per unit frequency bin, $f_\nu = \text{Const.}$ The flux density was obtained by dividing the Ly α flux by EW (observed), $f_\lambda = F(\text{Ly}\alpha)/W_{\text{obs}}$. Then the IGM absorption was calculated by assuming the redshift of $z = 4.11$ to obtain the continuum component of the spectrum expected at the redshift of the radio galaxy. The UV continuum contribution to the photometry was calculated by convolving the flat-continuum spectrum with the filter response curves. The IGM absorption on the Ly α line is included in the escape fraction, f_{esc} used in generating the mock catalogue of LAEs (see Orsi et al. 2008). Then sufficiently narrow line profiles (i.e., narrower than the $IA624$ passband) was convolved with the filter response curves, and the line contribution to the photometry was obtained.

Adding the contributions from both the Ly α line and the UV continuum, we calculated the R - and $IA624$ band magnitudes to apply the colour constraints. Since our calculation gives exactly the same continuum colour for all sources, we did not apply the constraints on the $B-R$ colour. This does not affect our results because the mock LAE catalogue does not contain any foreground contamination. Furthermore, the B -band magnitude cannot be predicted from our calculation with sufficient reliability, because we are assuming a very simple IGM absorption model. Since the BR magnitude used for the observed data is almost the same as R for high-redshift sources, we thus used the R -band magnitudes, instead of the BR . The colour constraints for the mock LAE sample are thus:

$$20 < IA624 < 26.6 \quad (5)$$

$$R - IA624 > 0.3 \quad (6)$$

$$R - IA624 > (BR - IA624)_{4\sigma}. \quad (7)$$

For the significance level of the *IA624* excess, $(BR - IA624)_{4\sigma}$, the same value as in eq. 4 was used to match the observed sample. For the comparison with the observed samples, we applied the magnitude cut of $IA624 < 26.6$ for eq. 5, and the observed *IA624*-excess threshold of $(BR - IA624)_{4\sigma}$. In total we select 30,012 model LAE sources in a comoving volume corresponding to $(500 h^{-1} \text{Mpc})^3$.

4 RESULTS AND DISCUSSION

4.1 Density field

4.1.1 The high density region around the radio galaxy

We quantified the difference between the TNJ1338 and SXDS fields by constructing their LAE surface density maps. We smoothed the spatial distribution of the LAEs with a Gaussian kernel with a radius (half width at half maximum, HWHM) of $4 h^{-1} \text{Mpc}$ (projected comoving distance at $z = 4.1$), and counted the number of LAEs within the same radius at each grid point, with a grid spacing of $0.5 h^{-1} \text{Mpc}$. Then the surface density was obtained by dividing the number by the area of the Gaussian aperture with the HWHM of $4 h^{-1} \text{Mpc}$. In deriving the average surface density, the areas within $5 h^{-1} \text{Mpc}$ of the edge of the FoV were flagged to avoid underestimating the surface density near the field edges. The kernel size was chosen based on the typical separation between the sources. We measured the distance to the nearest source for each LAE in our sample, and chose the smoothing kernel size to include ~ 68 percent of the whole sample. We confirmed that different sizes of the smoothing kernel also give a similar density distribution.

The density maps we obtained are shown in the Fig. 4. We can clearly see that the region around the radio galaxy is strongly overdense, and equivalently strong density peaks are not seen in the SXDS field. The density peak in the TNJ1338 field is $\gtrsim 4$ times the density averaged over the field ($1 + \delta_{\text{LAE}} = 4.13$ when the density is normalised with the average within the field), while the maximum peak in the SXDS field is only $1 + \delta_{\text{LAE}} = 2.36$. We then estimated the uncertainty of the density with this smoothing scale by computing the standard deviation of the density map of the SXDS field, determining the 1σ dispersion in δ_{LAE} as 0.47. The radio galaxy TNJ1338 is located in the densest region in the field, with $1 + \delta_{\text{LAE}} = 3.46$ at its position. The peak density is $1 + \delta_{\text{LAE}} = 4.13$, located $2.57 h^{-1} \text{Mpc}$ offset from the position of the radio galaxy. This overdensity can be traced on $\sim 10\text{--}20 h^{-1} \text{Mpc}$ scales around the radio galaxy. Outside this region, in contrast, the density appears to drop quite rapidly: on the northwestern side of the field there is a strongly underdense region just $\sim 20 h^{-1} \text{Mpc}$ from the density peak. Such a strong variation in the density of LAEs is not seen in the SXDS field. Although the overdensity of the TNJ1338 field had previously been suggested by Venemans et al. (2002), their FoV was much smaller than ours, and they were forced to estimate the overdensity (a factor of $\sim 3\text{--}5$) through comparison to a separate field survey at a similar redshift (Rhoads et al. 2000). With our wide-field imaging of this field, we have not only confirmed the overdensity by comparing with an identically-observed control field, but have also determined the spatial scale and structure of the overdense region.

Table 2. Statistics of the observed density field

Field	Mean ^a [$h^2 \text{Mpc}^{-2}$]	Percentiles ^b					G ^c
		10	25	50	75	90	
TNJ1338	0.0209	0.05	0.44	0.95	1.32	1.90	0.415
SXDS	0.0204	0.40	0.66	0.97	1.29	1.68	0.268

^aMean surface density over the field in comoving scale.

^bIn units of the normalized density ($1 + \delta_{\text{LAE}}$).

^cGini coefficient of the density distribution.

The difference between the TNJ1338 field and SXDS control field becomes clearer when comparing their density histograms, as shown in Fig. 5. In the SXDS field the distribution is concentrated near the average value, while the TNJ1338 field shows a much broader distribution extending toward both high- and low densities. In order to quantify the difference between the distributions in these two fields, we first compared the 10- and 90 percentiles for the density maps of the two fields. The upper panel of Fig. 5 shows the cumulative density distributions for the two fields, together with the percentiles. The statistics of the two fields are also summarised in Table 2. The TNJ1338 field has a wider density distribution compared with the SXDS field, especially at the lower-density end. The 10 percentile for the TNJ1338 field is $1 + \delta_{\text{LAE}} = 0.05$, which is 80 times lower than that of the SXDS field. The ratios of the two percentiles, i.e., the dynamic range of the density, for the TNJ1338 and the SXDS fields are 38 and 4.2, respectively. The TNJ1338 field has thus nearly an order of magnitude higher range in galaxy density than that seen in the SXDS field. The difference becomes even more obvious when we look into the highest- and the lowest-density bins: e.g., $1 + \delta_{\text{LAE}} < 0.01$ corresponds to the lowest 2 percent of density cells in the TNJ1338 field, while in the SXDS field only ~ 0.04 percent of the total grid points have such a low density.

A useful statistic to quantify the range of the density distribution is the Gini coefficient of the density field. The Gini coefficient, G , measures how uniformly LAEs are distributed within the field, and takes a value of $0 < G < 1$. The G value corresponds to the area surrounded by the two Lorentz curves corresponds to the given distribution and $G = 0$ (shown in Fig. 5). If all the LAEs are concentrated within one grid point, then G is unity. If the LAEs are distributed uniformly over the field, then G is zero. The Lorentz plot shown in Fig. 5 clearly shows that the TNJ1338 field has much higher G than the SXDS blank field, and the blank field agrees well with the simulation. The Gini coefficients of the density maps were calculated to be 0.415 (0.268) for the TNJ1338 (SXDS) field. This difference shows that the LAEs are more concentrated into high-density regions (especially into the high-density peak around the radio galaxy) in the TNJ1338 field, compared with the SXDS field. Together these statistics suggest that the galaxy density in the TNJ1338 field traced with LAEs is highly concentrated within the high-density region near the radio galaxy, but that there are also unusually low-density regions in the field where the number of LAEs is highly suppressed. This is quite different from the density field in the SXDS field.

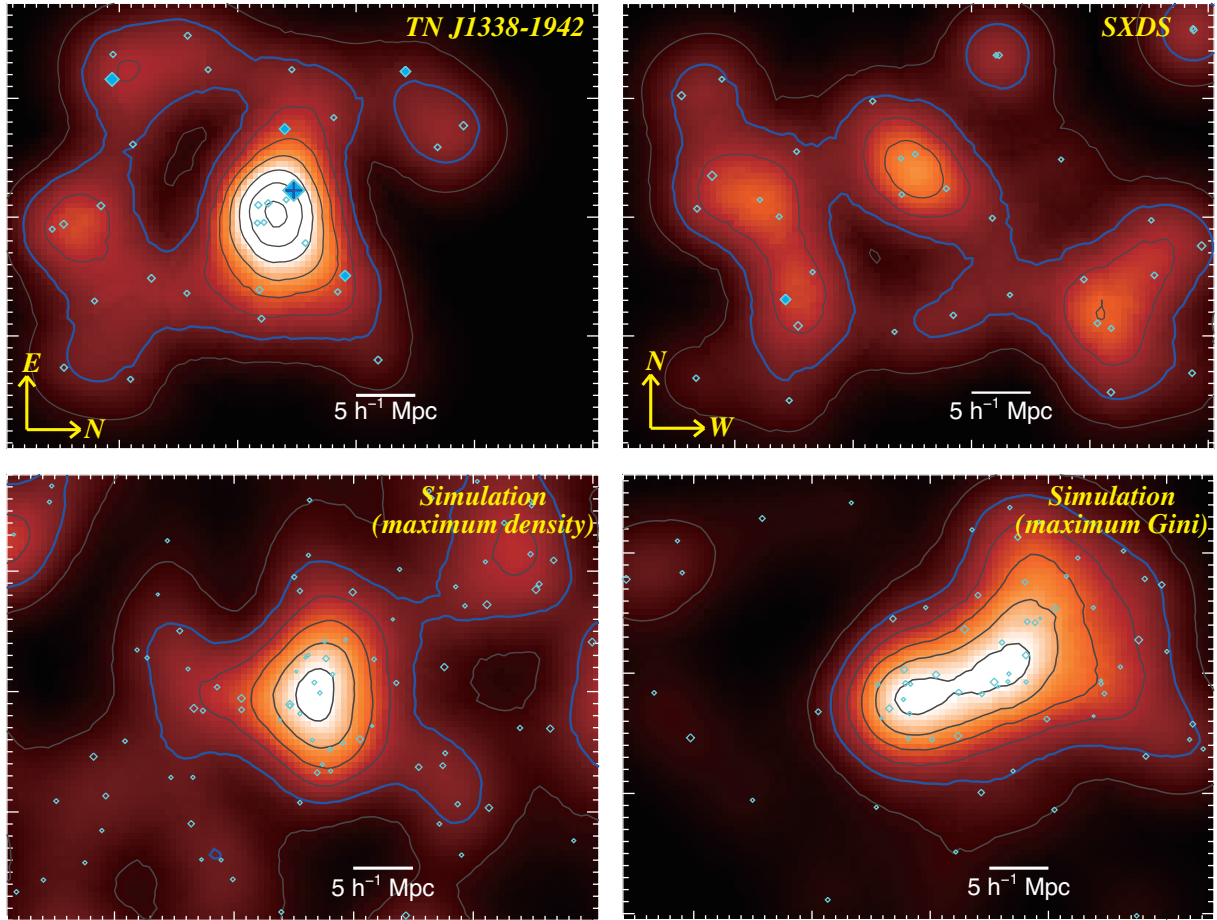


Figure 4. A comparison of the density field of LAEs. The top panels are the observed density map of the TNJ1338 field (left), and the SXDS field (right). The position of the radio galaxy TNJ1338 is shown with the blue cross mark near the density peak. The bottom panels are simulated density maps generated from the mock LAE catalogue using the same selection as those applied to the observed data, showing the same FoV centred on density peaks which are higher than that measured at the position of the radio galaxy: the field around the maximum density peak (left) and the field with the highest Gini coefficient (right). Each panel shows the $50 \times 38 h^{-2} \text{Mpc}^2$ (comoving) field. The contour interval is $0.5 \times$ the average density, with a lowest contour of 0.5 ($\delta_{\text{LAE}} = -0.5, 0.0, 0.5, 1.0, \dots$). The thick blue contour traces the average density over the field ($\delta_{\text{LAE}} = 0$). The cyan diamonds mark the positions of LAEs, and the sizes of these symbols represent the $\text{Ly}\alpha$ luminosities. The sources with $\log(L_{\text{Ly}\alpha} [h^2 \text{erg s}^{-1}]) \gtrsim 43.8$ are marked with filled symbols.

4.1.2 Density contrast within the TNJ1338 field

Although the TNJ1338 field has a very large dynamic range in LAE density, the average density of this field over the FoV of Suprime-Cam is still almost the same as that of the SXDS field. The average surface density of LAEs for these two fields are $0.0209 h^2 \text{Mpc}^{-2}$ and $0.0204 h^2 \text{Mpc}^{-2}$ for the TNJ1338 and the SXDS field, respectively. This suggests that the density traced by LAEs is almost uniform within 2.5 percent at $\sim 50 h^{-1} \text{Mpc}$ scales, when the density field is averaged over $\sim 160 \text{Mpc}$ along the line of sight (both in comoving scale). Even with this smoothing, there is a significant overdensity around the radio galaxy, and a similarly significant underdense region just adjacent to it. This “void” region next to the high-density region correspond to the peak of the density distribution near zero in the histogram (Fig. 5). The shape of this distribution is quite different from that for the SXDS field.

Due to the limited number of sources, ~ 30 in each field, it is not clear whether the underdense region is truly a void. However, the detectable (i.e., bright and large-EW)

LAEs were not found in this region, especially in the north-western quarter of the field. This appears to be a real effect since there are no bright stars in this region that would significantly affect the detection and photometry, as seen in the Fig. 3. Such a large underdense region is not seen in the SXDS field, again showing that this radio galaxy field has an unusually high density contrast. The real density contrast in this radio galaxy field is possibly higher than estimated, since we are smoothing the spatial distribution along the line of sight as a result of the relatively wide redshift coverage of the *IA624* filter. Although the apparent contrast would be enhanced due to the redshift-space distortion if the high-density region is actively accreting the material, such an effect is thought to be small because of the wide redshift coverage.

Such a large density contrast within a single field suggests that the high-density region around the radio galaxy is attracting material from well within the scale of the Suprime-Cam FoV ($38 \times 50 h^{-2}$ comoving Mpc^2 on the sky, when the edges are flagged out), because the average density

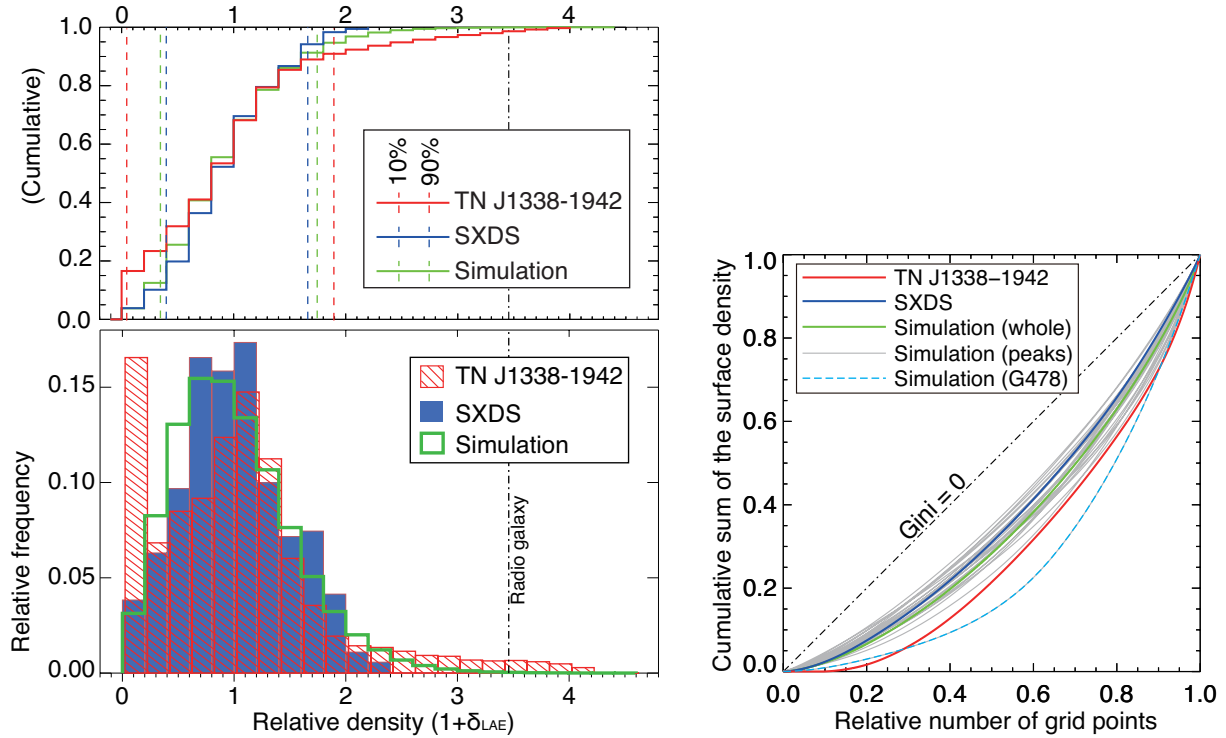


Figure 5. The statistics for the LAE surface density distribution. (Left) A comparison of the LAE surface density distributions for the two fields. The red hatched and the blue filled histograms show the density distribution for the TNJ1338 field and the SXDS control field, respectively. Overplotted with the thick green line is the histogram for the simulated density map obtained from the mock LAE sample. The vertical black dot-dashed line shows the density calculated at the position of the radio galaxy. The cumulative distributions are shown on the top panel. The red, blue and green lines denote the TNJ1338, the SXDS and the simulated map, respectively. The 10-th and 90-th percentiles are shown with the vertical dashed lines with the corresponding colours. We can see that the density distribution in the TNJ1338 field is much wider than that in the SXDS. The simulated density distribution is closer to the SXDS than to the TNJ1338 field. (Right) Lorentz curves for the density distribution. The normalised cumulative distribution is plotted against the normalised number of the grid points. The red, blue and green curves show the TNJ1338, the SXDS and the simulated map, respectively. Again the simulated distribution is closer to that of the SXDS field rather than the TNJ1338 field. The grey curves denote the 25 fields centred at the high-density peaks found in §4.3.1. The “G478” field shown with the cyan dashed curve is one of the 25 high-density fields with exceptionally high Gini coefficient, $G = 0.478$. Except this G478 field, the TNJ1338 field has much higher G than any high-density fields found in the simulation.

is almost the same as the blank field. If LAEs are tracing the matter distribution, then the surrounding dark haloes within this scale should have been merging into this overdensity. Since we do not have spectroscopic data for all the sources, we cannot draw any clear conclusions on the true spatial structure of the overdensity based solely on our current observations: it is not clear whether the density peak represents a single extremely overdense halo, or a less overdense filamentary structure elongated toward the line of sight (the latter case includes the case that two or more clumps are aligned along the line of sight). Nevertheless, the density contrast must have grown to a level high enough to form such a high density peak and a large void region. Even for the latter case, the high-density filament must have accreted material from its surroundings and grown to a sufficient length to evacuate the void region. Hence in both cases, the spatial extent of the high-density region should be fairly compact (or the filament should be narrow), as the TNJ1338 field shows a large void fraction and the high-density region extends only up to $\sim 20 h^{-1}$ comoving Mpc scales.

This requires that matter is concentrated into a high-density region of $\sim 10\text{--}20 h^{-1}$ Mpc (comoving) size, well

before the observed epoch of $z \sim 4.1$. Such a concentration should affect the star-formation and AGN activity of galaxies within the overdensity, in the form of, e.g., frequent galaxy mergers. This may therefore lead to an excess of massive galaxies harbouring active star-formation and/or AGN activity. The corresponding high matter concentration will also lead to a higher rate of gas accretion from the surrounding environment, again resulting in the enhancement of star-formation and AGN activity.

4.2 Luminosity function

4.2.1 Comparison with the blank field

As described above, we have found that the TNJ1338 field has a high density region around the radio galaxy, and a strong density contrast between this and the large void region just adjacent to the peak. To investigate the variation in the LAE LF Fig. 6 compares the $\text{Ly}\alpha$ LFs of the LAEs in the TNJ1338 and the SXDS fields. We can see that the faint-end slope of the LF in the TNJ1338 field is shallower than the SXDS, below a $\text{Ly}\alpha$ luminosity of

$\log(L_{\text{Ly}\alpha}[h^2 \text{ erg s}^{-1}]) \sim 43.6$. On the other hand, the LF in the SXDS field increases nearly monotonically down to our completeness limit, $\log L_{\text{Ly}\alpha} \sim 43.1$ (corresponding to $\log L_{\text{Ly}\alpha} \sim 42.8$ assuming $h = 0.7$), as the L^* is still slightly below the faintest data point (Ouchi et al. 2008, hereafter O08). In the TNJ1338 field, a similar trend can be seen in the LF for LAEs within the overdense region. We plotted the LF of the subsample of LAEs lying within regions with densities higher than the average of the whole Suprime-Cam field ($\delta_{\text{LAE}} \geq 0$). The faint end of this LF agrees with that of the SXDS field, but has higher values than in the SXDS by up to an order of magnitude. Note that the radio galaxy itself ($\log L_{\text{Ly}\alpha} \approx 45.0$) is excluded in the LFs plotted here. The LAE population in the TNJ1338 field is thus thought to be highly biased to bright sources, and the fraction of faint LAEs is reduced in this field. The shape of the bright end may suggest that our LAE sample consists of two different components, e.g., star-forming galaxies dominating the faint end, and AGN hosts dominating the bright end.

We have also compared the SXDS control sample with a narrowband-selected LAE sample at a similar redshift in the same field, to check the reliability of our control sample. The LF of the SXDS control sample agrees quite well with the LF of the narrowband-selected LAE sample at $z \simeq 3.7$ (O08), down to the completeness limit ($\log(L_{\text{Ly}\alpha}) \sim 43.1$). Since the bandpass of the *IA624* filter is several times larger than the *NB570* narrowband filter, the survey volume is comparable to that of O08, even with only one FoV of Suprime-Cam. This reduces the field-to-field variance, as the density fluctuations are smoothed out along the line of sight. Thus we confirmed that our SXDS sample is a valid control sample in terms of LF, representing the typical number density of LAEs at $z \sim 4$. The LF in the TNJ1338 field, on the other hand, lies beyond the variance expected from the results of O08. At the brightest end of the LF, $\log L_{\text{Ly}\alpha} \gtrsim 44$, we did not find any sources in the SXDS field, while we still found sources in the TNJ1338 field even when we exclude the radio galaxy itself. Such bright sources are almost never seen in blank-field surveys for LAEs at similar redshifts (Dawson et al. 2007; Ouchi et al. 2008).

These results reinforce the idea that the TNJ1338 field is unusual, not only in terms of the overdensity of LAEs, but also the Ly α LF. Since our *IA624* data is deeper in the TNJ1338 field than in the SXDS field, this should not be due to the difference in the completeness. We mentioned in §4.1.2 that the density contrast in this field implies that the high-density region is accreting material from well within $\sim 50 h^{-1} \text{ Mpc}$ scale. At this scale, such accumulation of the material is likely to be affecting the star-formation activity in galaxies and hence galaxy formation and evolution, leading to a change in the LF. This suggestion is also supported by comparing the UV LFs of these two fields (Fig. 6 right). The UV LF of the TNJ1338 field shows significant enhancement at the very bright end ($M_{\text{UV}} \lesssim 22.7$), while at $M_{\text{UV}} \gtrsim 21.5$ the number of galaxies is relatively suppressed. If we derive the UV LF from LAEs only within the overdense regions, the faint end of the LF appears to agree with that in the SXDS field within the errors.

We should note that the samples in both the TNJ1338 and SXDS fields have relatively low completeness at the faint end. Our LAEs are selected based on the intermediate-band filter images, so that the samples are biased to sources with

large EWs. This results in a relative faintness of the UV continuum in these systems. Indeed, about half of the both samples have very faint UV continua, often below 3σ , and as a result the UV LFs shown in Fig. 6 are based on 14 and 19 sources for the TNJ1338 and SXDS fields, respectively. As a result the size of the magnitude bins is large (2 mags) and the shape of the LFs are thus heavily smoothed. However, the two data points of the SXDS control sample at $M_{\text{UV}} \lesssim -21$ show fairly consistent values with the $z \sim 3.7$ SXDS sample of O08, so that we can make a meaningful comparison between the two fields in this luminosity range. Within this range, the bright-end shape of the UV LF is much flatter than that in the SXDS field, which is a similar trend to that seen in the Ly α LF, although the errors are large. The shape of the UV LF in this field is very flat, and apparently not Schechter-like at this luminosity range. The formation of actively star-forming galaxies, as well as AGNs, are thus likely to be enhanced in the TNJ1338 field, which host the extremely high-density region.

4.2.2 Implications for galaxy formation

The high-density region around the radio galaxy is so unusual that it faces the large void region. The material originally in the void region must have moved into the surroundings by the epoch of $z \simeq 4.1$, and among the “surroundings”, the high-density region around the radio galaxy is the most prominent peak. This suggests that some large fraction of the material originally in the void region may have travelled to the vicinity of the radio galaxy. Then, how well can this scenario account for such a high density contrast as we found? We made a rough estimate to test this scenario. The separation between the density peak and the void region is $15 - 20 h^{-1} \text{ Mpc}$ in comoving scale, which corresponds to $\sim 4 - 6 \text{ Mpc}$ in physical scale at $z = 4.1$. If the material travelled this distance within a Hubble time at this redshift, the velocity is required to be $\sim 4 - 6 \times 10^2 \text{ km s}^{-1}$. This is although a very naive estimate, as is just the velocity required to travel linearly from the centre of the void to the density peak. In terms of the void evolution, the required velocity is slightly smaller: the apparent radius of the completely empty void is $r \sim 2 - 3 \text{ Mpc}$, leading to the peculiar velocity at the edge of the void is around $\frac{1}{3} H(t)r \sim 2 - 3 \times 10^2 \text{ km s}^{-1}$. These values are well below the typical velocity dispersion of the present-day (virialised) galaxy clusters. Although the required peculiar velocity may be larger than this because the distance assumed here is just the projected distance, the high-density region can be to some extent responsible for accreting the material initially in the void region.

It is however quite unlikely that all of the material initially in the large void had been simply accreted onto the high-density region by the epoch of $z \simeq 4.1$. The material should in principle flow out in all directions from the centre, so that the single overdense region cannot be fully responsible for the formation of the void. The simplest interpretation for the observed (apparent) density contrast is that the initial density fluctuation is quite large, and the contrast had existed since an epoch well before $z \simeq 4.1$. Another interpretation is the enhancement of star-formation activity within overdense regions (e.g. Steidel et al. 2005; Koyama et al. 2013), leading to the enhancement of actively star-forming galaxies possibly dominating the bright end of the LF. This

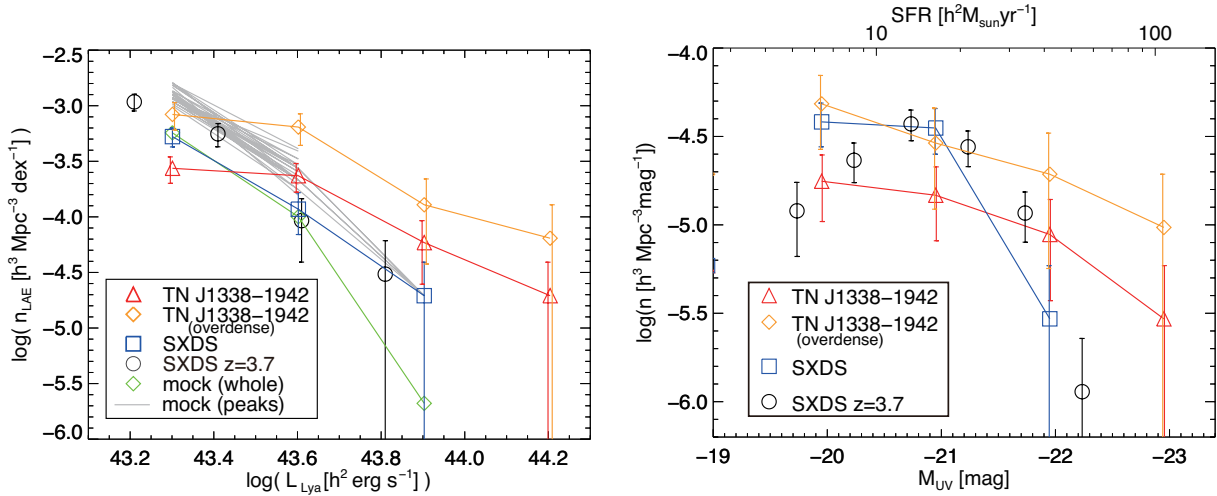


Figure 6. (Left) The Ly α luminosity function (LF) of the observed samples of LAEs. The red triangles show the LF of the total LAE sample in the TNJ1338 field. The subsample lying within the overdense regions (higher than the average of the field) is shown with the orange diamonds. The blue squares denotes the SXDS control sample. The black circles shows the LF of $z \simeq 3.7$ LAEs in the SXDS field, taken with a narrowband filter (Ouchi et al. 2008). The green diamonds show the LF of the mock LAE catalogue by Orsi et al. (2008), and the grey lines show the LF derived from the subsample of the mock LAEs residing within the Suprime-Cam-sized fields centred at the positions of 25 highest-density peaks. The radio galaxy TNJ1338 is omitted to show the luminosity range of the normal LAEs. Note that the data points are slightly shifted to improve the visibility. We can see that the number of bright LAEs is enhanced in the radio-galaxy field, and the fraction of the faint LAEs is reduced. The LF within the overdense regions has almost the same shape as that within the whole field, but the absolute number density agrees with that in the SXDS at a luminosity of $\log(L_{\text{Ly}\alpha} [\text{h}^{-2} \text{erg s}^{-1}]) \sim 43.3$. (Right) UV luminosity functions. The symbols are same as the left panel. The LF for the LAEs in our field appear to be enhanced at the bright end, while being relatively suppressed at the faint end. Note that the lowest luminosity bin shown here has low completeness. The mock sample is not shown here since the UV LF is still not well calibrated with Ly α -selected galaxies.

may result in a drastic enhancement of the galaxy bias for bright sources. The excess of extreme starbursts within protoclusters found in some observational studies (e.g. Blain et al. 2004; Capak et al. 2011; Ivison et al. 2013) is consistent with this idea. Because of the lack of spectroscopic data, we cannot discriminate between star-formation and AGN activities. It is thus also possible that AGNs are dominating the bright end of the LF, which is highly enhanced in the radio galaxy field. Such an enhancement of AGN activity in overdense environments has been found observationally in some cases (e.g. Pentericci et al. 2002; Croft et al. 2005; Lehmer et al. 2009; Digby-North et al. 2010). Since our samples are relatively biased to bright LAEs, such effects will enhance the apparent density contrast.

The difference between the LFs in the two fields depends strongly on the luminosity. When we examine the LF for the overdense regions in the TNJ1338 field, the difference for the luminosity range $\log L_{\text{Ly}\alpha} \gtrsim 43.6$ (corresponding to the brightest two data points for the SXDS field: $\gtrsim 43.3$ if $h = 0.7$ is assumed) is about an order of magnitude. This luminosity range contains 17 sources for the TNJ1338 field (all in the overdense regions), while only 7 lie within this range in the SXDS field. On the other hand, both LFs agree with each other within their error bars (factor of ~ 1.6) at $\log L_{\text{Ly}\alpha} \sim 43.3$. The difference in the faintest data point roughly corresponds to the difference in the total number density for the two fields (the whole SXDS field and the overdense region of the TNJ1338 field). We estimated that the mean density within the overdense regions shown here is ~ 1.6 times the average of the SXDS, corresponding to $\delta_{\text{LAE}} \sim 0.6$. Since the LF for the overdense regions in

TNJ1338 exceeds the LF in the SXDS field by an order of magnitude on the bright end, the overdensity of the bright ($\log L_{\text{Ly}\alpha} \sim 43.9$) LAEs is $\delta_{\text{LAE}} \sim 5$ or so. This means that, if we assume the galaxy bias for LAEs at $\log L_{\text{Ly}\alpha} \sim 43$ to be $b \sim 2.4 - 4$ (e.g. Ouchi et al. 2005, 2010; Kovač et al. 2007; Chiang et al. 2013), and the faint LAEs are correctly tracing the matter density of this field, the bias for brighter LAEs must be $b \sim 20 - 40$.

Such a strong luminosity dependence of the bias seems to be rather different from the prediction of the model of Orsi et al. (2008), which predicted only a modest dependence of bias on LAE luminosity. This may suggest that the bright end of the LF is dominated by populations other than the normal star-forming galaxies included in that model, such as hosts of AGN or AGN-induced star-formation activities. However, it is still not clear if this result is truly against the prediction. The bias measurement of Orsi et al. (2008) is based on clustering on large scale, so that the results are different from ours. Furthermore, their Fig. 6 shows large uncertainty on the bias at the very bright end of the model LAEs, $\log L_{\text{Ly}\alpha} \sim 43 - 43.3$, and it is still possible that the bias of such bright LAEs depends strongly on the luminosity, even for the model LAEs. Orsi et al. (2008) did not present predictions of the clustering bias for LAEs brighter than $\log L_{\text{Ly}\alpha} \sim 43.3$, because their simulation did not contain enough such LAEs for an accurate measurement on large scales.

We here showed only the simplest estimate of the galaxy bias, since we are heavily affected by small number statistics due to having only ~ 30 LAEs in each field. We cannot probe the scale-dependence of the galaxy bias either: the bias

estimated above is on a comoving scale $\sim 20 - 30 h^{-1} \text{Mpc}$, which corresponds to the area inside the contour of average density in Fig. 4. Note again that this is smoothed over $\sim 160 h^{-1}$ comoving Mpc along the line of sight. We can then qualitatively say that there apparently exists a large density contrast within $\sim 50 h^{-1}$ comoving Mpc scale around the radio galaxy TNJ1338, apparently enhanced to some extent by highly biased nature of the bright LAEs including AGN hosts.

4.3 Comparison with the mock catalogue

4.3.1 Density field of the whole simulated map

We compared the density field shown in §4.1 with the mock LAE sample, and evaluated the density distributions of the TNJ1338 field, as well as the control field. The simulated density maps are obtained by applying the same analyses to the mock LAE catalogue described in §3.3. We used the same smoothing radius, $4 h^{-1}$ comoving Mpc, in this process. The simulation covers a comoving volume of $(500 h^{-1} \text{Mpc})^3$. Our *IA624* filter covers a radial comoving distance of $\approx 160 h^{-1} \text{Mpc}$, so that we can obtain three independent slices perpendicular to the line of sight to create mock sky distributions of LAEs. After selecting the LAEs with similar colour constraints to the observed samples, we extracted the LAEs within a slice of thickness (distance along z -axis of the simulation box) of $160.5 h^{-1} \text{Mpc}$, and projected them onto the xy -plane. In this process we took account of the effect of redshift-space distortions. The redshift-space coordinates were computed by taking the z axis as the line-of-sight direction, adopting the distant observer approximation. We then smoothed the spatial distribution of LAEs projected on the xy -plane, and counted the LAEs within a smoothing radius centred at each grid point. The simulated LAE density map covers ~ 100 times larger area for each slice than a single pointing of the Suprime-Cam, and thus ~ 300 times larger volume for the 3 slices together.

We first used this whole simulated map to compare the density distribution with the observational data. Fig. 5 shows the density histogram of the whole simulated map, overlaid on the observed density histograms. We see that the density distribution of the simulated map is at least qualitatively consistent with that of the SXDS field. The distribution is close to Gaussian with a slightly longer tail toward the high density, peaked around the mean density. The peak amplitude and the width of the peak both look close to that of the control sample. At higher density, on the other hand, the simulated map has a longer, more extended tail than that of the control sample. This looks still consistent with the control sample, because the field coverage of the observational data is much smaller than the simulation. However, the high density tail seen in the TNJ1338 field is larger than that in the whole simulated map.

Statistical tests also support this difference between the SXDS and TNJ1338 fields, in terms of the comparison with the simulated map. The 10- and 90 percentiles of the density in the simulated map are 0.35 and 1.74 respectively, and the ratio between the two percentiles is 5.0, which is closer to that in the SXDS (4.2) than in the TNJ1338 field (38.0): see Fig. 5 left. We also calculated the Gini coefficient of the simulated density map, $G = 0.306$, and compared with

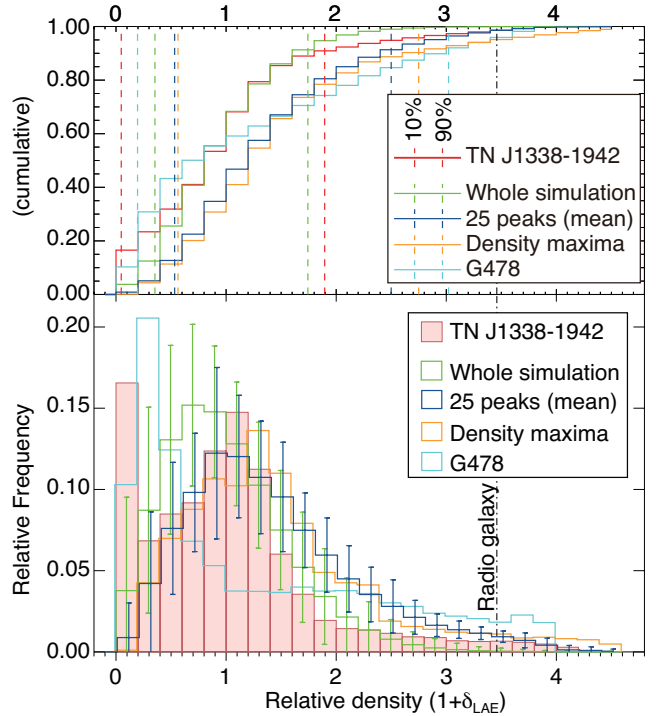


Figure 7. Comparison of the density distributions between the TNJ1338 field and the simulated map with various conditions for the simulation. The filled red histogram shows the observed density distribution of the TNJ1338 field (the same as in Fig. 5 left). The green outlined histogram is the density distribution for the whole simulation volume. The errors were estimated by computing the density distributions for 300 different Suprime-Cam-sized fields centred at random points, calculating the standard deviation for each density bin. The blue outline is the averaged distribution for the 25 fields centred at density peaks higher than the density measured at the radio galaxy position. The orange outlined histogram is for the one out of the 25 fields with the highest peak density, and the cyan outlined histogram is for that with the highest Gini coefficient (G478 field). The cumulative distributions are shown in the top panel, together with the 10- and 90-percentiles. The histograms are slightly shifted along the x axis to improve the visibility. The large fractions of pixels in the highest- and the lowest-density bins cannot be simultaneously reproduced with the simulated density map within the errors. Although the high-density regions can be reproduced at the peak positions, the high volume fraction of the void regions is not seen around typical peaks. The G478 simulated field reproduces both the large void fraction and the high density tail seen in the TNJ1338 field, but the peak in the density distribution around the average density seen in the TNJ1338 field is not reproduced by this G478 field.

the observed distributions in the two fields (Fig. 5 right). The dynamic range of the LAE density for the simulated map is thus in between those of the two observed fields, and closer to the SXDS field than the TNJ1338 field. We then assume that the SXDS field has a typical density distribution of LAEs at $z \sim 4$, and we can evaluate how rare the high-density region seen in the TNJ1338 field is. The density measured at the position of the radio galaxy is $1 + \delta_{\text{LAE}} = 3.46$. Such high density regions are quite rare in the simulated map, corresponding to the densest 0.06 percentile of the whole volume, while the same overdensity corresponds to the 1.8 percentile of our survey volume in the TNJ1338 field.

It is also important to check the size of field-to-field variations within the simulation volume. To do this, we first obtained density maps centred at random positions. We selected 100 positions in each of the three slices within the central $440 \times 440 h^{-2} \text{Mpc}^2$, and made density maps within a FoV of Suprime-Cam centred at these 300 points. Then we calculated the standard deviation for each bin of the density distribution using the 300 maps. Fig. 7 shows that the observed density distribution, especially the density contrast within a single field, is very different from that for the simulated map as a whole. The volume fraction within the medium- to high-density ($1 + \delta_{\text{LAE}} \sim 1 - 2.5$) bins in the TNJ1338 field agrees with that obtained from the whole simulation volume, at 1σ level. On the other hand, the relative frequencies for the lowest- and the highest-density bins do not agree with those for the simulated map. This also suggests that such extreme overdensities / underdensities as we found observationally are quite rare in the simulation: the random sampling in the simulated map is unlikely to reproduce the unusual density distribution observed in our field. In fact, we found only 25 density peaks higher than that measured at the radio galaxy position, over the whole simulated map. This is comparable to the number density of Coma-type protoclusters identified in the same simulation (58 protoclusters: Chiang et al. 2013). The number (25 peaks) corresponds to number density of $6.9 \times 10^{-8} \text{Mpc}^{-3}$ in comoving units ($9.1 \times 10^{-6} \text{Mpc}^{-3}$ in physical units). This number density is also comparable to that of known bright radio sources at $z > 2$ (see the section below). However, most of these peaks do not seem to reproduce the high density contrast seen in the TNJ1338 field. This suggests that high-density regions that host powerful radio galaxies associated with a giant Ly α nebulae, like our observed field, should be much rarer than this.

4.3.2 Density fields around the high-density peaks

Next we checked the density distributions around the 25 density peaks found in the simulated map. In order to obtain the density distribution in the same manner as the observed data, we extracted the LAEs within a single Suprime-Cam FoV centred at the peak positions. Then we made the density maps in these fields, and calculated the density distributions using the grid points within the central $40 \times 27.5 h^{-2} \text{Mpc}^2$, similarly to the analyses for the observed LAE sample. Fig. 7 also shows the average density distribution of the fields around the 25 density peaks, together with the errors. This average distribution is shifted toward higher density compared with the whole simulated map, smoothed along the density axis. However, the shape of the distribution does not significantly change: it agrees very closely with that of the whole map if we normalise the density with the average within these 25 fields, instead of the average of the whole simulated map. The distribution again seems to be different from the distribution in the TNJ1338 field, although the high-density tail is reproduced well. This implies that high-density regions just adjacent to the void regions, like we observed, are still much rarer than simple high-density peaks.

To further analyse the density distribution, we calculated the Gini coefficient for each map centred at the 25 high-density peaks. Fig. 5 shows the comparison of the Lorentz

curves for the observed- and simulated density maps. The ordinate corresponds to the cumulative sum of the abscissa of the left panel, normalised with the total sum of the LAE surface density measured at each grid point. This shows that, while the density distribution of the SXDS field is well within the scatter of the simulated map, the distribution of the TNJ1338 field is far from the simulated ones, even from those around the density peaks. The possible exception is one of the 25 fields, showing $G = 0.478$ (hereafter G478 field: Fig. 4 bottom-right panel). The peak density of G478 field is 3.98 times the average over the whole simulated map, and has a large fraction of void regions. The 10- and 90 percentiles of G478 field are 0.157 and 2.419, respectively, and the ratio of the two quartiles is 15.4. Although the distribution thus seems to be close to that of the TNJ1338 field, the G478 field does not completely reproduce the properties of the TNJ1338 field. The average density of the G478 field is 1.25 times the average over the whole simulated map, giving a peak density of $1 + \delta_{\text{LAE}} = 3.19$ when normalised with the average density within the field. The shape of the density distribution is also different: the density histogram of G478 does not have a peak around the average density (cyan histogram in Fig. 7).

These results together suggest that the density distribution of the G478 is roughly consistent with that of the TNJ1338 field, in terms of the density contrast within the field. The remaining differences might be explained in terms of changes in the galaxy-formation processes in such unusually high-density regions harbouring powerful radio galaxies. The simulation does not include Ly α radiation from AGN activity, which can introduce significant differences in the LF, even if the underlying dark matter structure is similar. We then roughly evaluated how well the G478 field reproduces the TNJ1338 field, in terms of the number density: we found no other G478-like fields within the whole simulation volume of $(500 h^{-1} \text{Mpc})^3$ (comoving). This corresponds to a comoving number density of $3 \times 10^{-9} \text{Mpc}^{-3}$ with very large uncertainty because we have only one such region in the whole simulation volume. This is two orders of magnitude lower than the number density of Virgo-type protoclusters identified in the same Millennium Simulation, and still an order of magnitude lower than Coma-type protoclusters (Chiang et al. 2013). The number density of radio galaxies in the universe at $2 < z < 5$ is observed to be a few 10^{-8}Mpc^{-3} (e.g. Venemans et al. 2007; Miley & De Breuck 2008), comparable to that of the Coma-type protoclusters. This means that the environment of the radio galaxy TNJ1338 is even rarer than the known radio galaxies at $z > 2$. In fact, not all the high- z radio sources have Ly α nebulae extended to $\gtrsim 100 \text{kpc}$ (van Ojik et al. 1997). Such extended Ly α nebulae should reflect exceptionally active interaction between the radio galaxy and its surroundings.

Note that we found only one field like G478 in the whole simulation volume, so the theoretically predicted number density of such high-density region remains significantly uncertain. The observational constraints are also very weak, since there are very few high- z powerful radio galaxies known to date, and the technique finding high- z radio sources, i.e., selecting based on ultra-steep radio spectra, will miss a significant fraction of high- z galaxies (e.g. Ker et al. 2012). Even larger simulations together with more realistic models for LAEs including AGN are needed to calculate

accurate statistics for rare density peaks like that in the TNJ1338 field, and to simulate the density field and the LF found around them. In addition, deep and large surveys for high- z radio sources are needed to more accurately estimate the observed number density of TNJ1338-like regions.

4.3.3 Density peak profiles

In order to test how well the simulated map reproduces the observed spatial distribution of the LAE density in the TNJ1338 field, we computed the radial overdensity profile of this peak, and compared with the simulated density map. Fig. 8 shows the comparison of the density profiles between the observed peak in the TNJ1338 field and high-density peaks in the simulated map. The leftmost panels show the observed density profile. As shown in 4.1.1, the peak density in the TNJ1338 field is $1 + \delta_{\text{LAE}} = 4.13$, and the radio galaxy position is slightly offset ($\sim 2.5 h^{-1}$ comoving Mpc) from the peak, at which the density is ≈ 84 percent of the peak. Although the redshift uncertainty is fairly large, we can roughly estimate the spatial scale wherein the high-density peak is accumulating the material from the surroundings, based on this profile. The radius of half-maximum is $\sim 6 h^{-1}$ projected comoving Mpc, and the average density within this radius is $1 + \delta_{\text{LAE}} \sim 3$. This could be produced by spherical collapse from a region with radius of $\sim 9 h^{-1}$ Mpc (comoving). Although this is a very rough estimate, it is clear that the accumulation of material is occurring well within our survey volume. The profile does not significantly change even when normalized with the average density over the SXDS field.

For comparison with this observed density peak profile, we selected the 25 high-density fields described above (including the G478 field). We found that none of these fields have peak density as high as the observed one when we normalised the density with the average *within* the same Suprime-Cam-sized FoV. We then applied the threshold for the peak density of $1 + \delta_{\text{LAE}} > 3.46$, which corresponds to the density at the position of the radio galaxy. Three out of the 25 peaks have their peak value higher than this threshold density. Fig. 8 shows the comparison of these three peaks with the observed profile of the TNJ1338 field. The observed peak density, $1 + \delta_{\text{LAE}} = 4.13$ when normalised with the average within the same field, cannot be seen in any of the three fields, Peak 1, 13 and 21, when we normalise the density in the same manner, although the half-maximum radii of these peaks are all comparable to that of the observed peak in the TNJ1338 field. This implies that low-density void region(s) within the same field, which are not seen in the simulation, are required to reproduce the *normalised* peak density.

Apart from the peak amplitude, the shape of the radial density profile seems to be roughly reproduced by the simulated map. When we normalise the density with the whole simulated map, the density profiles seem to show a better match with the observational data. The bottom row of Fig. 8 shows a comparison for this case. To make the fair comparison, the density around the observed peak is then normalised with the average of the SXDS field, although the difference is only 2.5 percent. Peak 1 gives the best match with the observed one in terms of the peak amplitude, but is more radially extended, with the $1 + \delta_{\text{LAE}} > 2$ level extending more than $12 h^{-1}$ comoving Mpc. Another two peaks are

relatively isolated, unlike Peak 1, but neither peak simultaneously reproduces the amplitude and the width observed for TNJ1338. If the normalization were different, these peaks might resemble the observed high-density region. Since we do not know the *true* mean LAE density of the universe, it is possible that the normalization is not correct. Even the SXDS field might be overdense, as the average density is almost the same as that in the TNJ1338 field. To evaluate this possibility, further wide-field observations, such as the Hyper Suprime-Cam survey, are needed especially for the control sample in blank fields.

There are at least three factors which might explain the difficulties in reproducing the density distribution observed in the TNJ1338 field. First, the selection of LAEs in the simulation does not exactly match the observational one. Especially for the broadband colours, we did not put any constraints to select the LAEs from the mock catalogue, possibly causing the difference in the selection function. However, this effect is unlikely to significantly change the resulting density distribution. Our mock LAE sample reproduces both the LF and the density distribution of the SXDS control sample quite well. Our selection of LAEs is thus thought to be working well at least for the faint end of the LF, where the TNJ1338 and the mock samples agree with each other. The second possibility is that the LAE model itself is not sufficiently realistic. For example, the escape fraction of Ly α photons is assumed to be constant for all the LAEs. If the escape fraction is changed in highly overdense regions by e.g. galaxy-galaxy interactions or AGN feedback, the spatial distribution of LAEs may significantly change in the field. This is also related to the third factor, i.e., the observations might include a significant contribution of Ly α coming from AGN, which is not included in the model. AGN activity may affect the galaxy-formation processes of the surroundings through, e.g., induced star formation (Zirm et al. 2005). Such AGN activity may be enhanced in overdense environments (e.g. Pentericci et al. 2002; Croft et al. 2005; Lehmer et al. 2009; Digby-North et al. 2010). If the bright LAEs in our TNJ1338 sample are predominantly AGN, this could lead to significant enhancement of the LAE number density, emphasizing the density contrast.

Another, much more naive interpretation is that the Millennium Simulation is not large enough to reproduce this kind of overdensity. This is in case if the halo mass of the overdensity is significantly larger than the maximum halo mass of the Millennium Simulation. Even if the SXDS field is suffering from overdensities and our density normalisation is not correct, such a steep and high density peak with large density contrast is not reproduced in the current simulation. The disagreement may be overcome by carrying out even larger simulations. The density profiles around massive haloes in such a large simulation may be different from those around less massive haloes: extremely massive haloes possibly form very high density peaks without significant growth in size of the overdense-regions.

In any case, more precise measurement of the density field and constraints on the AGN activity in our LAEs are needed to test the possibilities described here.

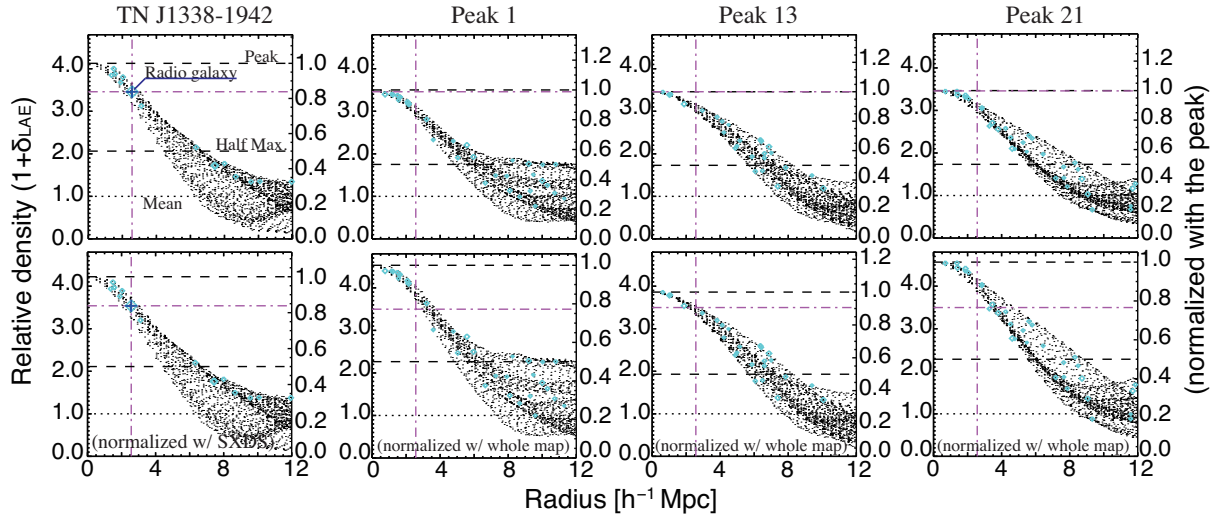


Figure 8. Overdensity profiles around density peaks. Relative overdensity is plotted as a function of the comoving distance from the peak. The leftmost column shows the observed density profile centered at the density peak observed in the TNJ1338 field. The profile in the top panel is based on the density normalised with the average over the FoV of Suprime-Cam in the same field. The density measured at the radio-galaxy position is shown with the blue cross. The bottom panel is based on that normalised with the average of the SXDS field. The remaining columns show the profiles of the density peaks found in the simulated map. For each panel, each black point corresponds to the measurement at a single grid point. The LAE positions are marked with cyan diamonds, with the symbol sizes representing the Ly α line luminosities. The mean density is shown by the dotted line, and the peak- and the half-maximum densities are shown by the black dashed lines. The density and the distance measured at the position of the radio galaxy are marked with the magenta dot-dashed lines. The right axis shows the density normalised with the peak value.

4.3.4 Luminosity function

Fig. 6 also shows the LF of the mock LAE sample. Again this sample is selected with the same colour constraints as the TNJ1338 sample. The mock sample has been already shown to have a Ly α LF reproducing well that of O08's sample (Orsi et al. 2008). This means that the mock sample is expected to reproduce the LF of our control sample. The LF of the mock sample agrees quite well with the control sample except for the bright end ($\log L_{\text{Ly}\alpha} \gtrsim 43.6$). The small difference from the O08's sample at the faint end is thought to come from the difference of the filter and the depth: our sample is selected based on the intermediate-band imaging, while O08 is based on the narrowband imaging. The colour constraints of our sample roughly corresponds to the rest-frame EW of $\gtrsim 70\text{\AA}$, while that of O08 corresponds to $\gtrsim 44\text{\AA}$. The differences in the band, as well as the exposure time, also lead to the difference in the sensitivities to the Ly α line. O08's sample is a factor of ~ 2 deeper than ours, so that the mock LF comes slightly lower than the O08's LF, as is also true for our control sample. The bright end of the LF was determined from a single source, and thus the LF of the mock sample is still consistent with that of the control sample within the large errors. Since the number of sources is much larger in the mock catalogue than in the SXDS sample, the mock LF may be correctly reproducing the LF of normal star-forming galaxies at this redshift, excluding AGN. The bright end of the LF is likely to be dominated by AGN as suggested in O08, and the single source found in the highest luminosity bin in the SXDS field is possibly an AGN host.

Similarly to the comparison with the blank fields, the LF in the whole TNJ1338 field is a factor of ~ 2 higher than the mock LAE LF at $\log L_{\text{Ly}\alpha} \sim 43.6$. For the fainter

range, the TNJ1338 LF comes below that of mock LAEs at $\log L_{\text{Ly}\alpha} \sim 43.3$. The crossing point is in between these two, i.e., the number of LAEs fainter than $\log L_{\text{Ly}\alpha} \sim 43.3 - 43.6$ seems to be suppressed in this field. The faint end of the LF agrees with the mock, when we look at the LF of the overdense regions in the TNJ1338 field. While the faint-end LF of this field does not show any enhancement compared to the mock LF, the bright end, $\log L_{\text{Ly}\alpha} \sim 43.9$, shows a large enhancement by one order of magnitude. This again suggests that the TNJ1338 field is a peculiar field dominated by bright LAEs, or AGN including the host of the radio galaxy. There are four bright LAEs contained in the two highest-luminosity bins ($43.8 \leq \log L_{\text{Ly}\alpha} \leq 44.4$) in this field, and such bright sources are likely to be hosting AGN, as suggested by O08. Such a population of bright LAEs, as well as the unusually high galaxy overdensity, should largely affect the galaxy-formation within this field.

The main differences between the TNJ1338 and the mock LAE samples in terms of LFs are then thought to be (1) the presence of the AGN, (2) the high-density peak as high as $1 + \delta_{\text{LAE}} \sim 4$, and (3) the large density contrast within a single FoV of the Suprime-Cam. Of these three, (2) can be partly reproduced with the mock sample as described in §4.3.1 and §4.3.3. We then tested how the LF differs from the observed one when one of these three main discrepancies are partly solved, by computing the LF within the peak regions seen in the simulated map. The resulting LFs in overdense regions show almost the same shape as the LF from the whole mock sample, and the amplitude of the LF becomes a factor of $0.2 - 0.4$ dex higher. We can see in Fig. 6 that only five out of the 25 high-density fields contain LAEs with $\log L_{\text{Ly}\alpha} \sim 43.9$. Even these five fields contain only one source each, but we can estimate the bright end of

the LF by averaging the 25 fields, $\log n_{\text{LAE}} = -5.41$ at the bright end. This value is only 0.27 dex higher value than the total mock sample. This means that there are no significant enhancements of the number (fraction) of bright LAEs such as we found in the TNJ1338 field. While the enhancements of the total number density of LAEs are relatively well reproduced in these high-density fields, the LF shape remains almost unchanged from that of the whole mock sample, i.e., not biased to bright sources.

Note that none of the three peaks described in §4.3.3, nor the G478 field described in §4.3.2, are included in the five fields containing the brightest LAEs. These five fields do not have extremely high G 's, only one of which exceeds 0.3. This simply means that the brightest LAEs are likely to be found in fields with high average density. This is also expected from the properties of the mock LAEs: the galaxy bias positively correlates with the Ly α luminosity $L_{\text{Ly}\alpha}$, but changes by only a factor of $\sim 2 - 3$ (Le Delliou et al. 2006; Orsi et al. 2008). On the other hand, the LFs of our *observed* samples suggest that the bias depends more strongly on $L_{\text{Ly}\alpha}$. The mock LAE sample does not contain AGN at all, so that it can reproduce only the properties of “normal” LAEs, not LAEs hosting AGNs, nor AGN-induced star formation. Activity related to such AGN, e.g., AGN-induced star formation in the vicinity of the radio galaxy (Zirm et al. 2005), may lead to enhancements of star-formation in this high-density region. Such interactions between the AGN and the surrounding environment may also occur further out from the central radio galaxy, as the extended Ly α nebula is observed up to ~ 100 kpc (Venemans et al. 2002), and some Ly α nebulae are aligned with the surrounding large-scale structure up to $\sim 10 h^{-1}$ comoving Mpc (Erb et al. 2011). Furthermore, three out of the four LAEs mentioned above in the highest luminosity bins, as well as the radio galaxy, lie within the overdense ($1 + \delta_{\text{LAE}} > 1$) regions. These may together suggest that star-formation / AGN activity is enhanced by the presence of AGN in the overdense regions, while there are no such sources of enhancement in the underdense regions.

Such an enhancement is expected from the high galaxy density, leading to frequent galaxy mergers. The high density may also lead to high gas accretion rates, which enhances the star-formation / AGN activity resulting in bright LAEs. These mechanisms will result in a large bias of the bright LAEs, dominating the bright end of the LF. Such a large bias for bright LAEs results in the large density contrast of bright LAEs described in §4.1.2. In order to see how such an enhancement affects the LF of *normal* star-forming galaxies in the overdense environment, we need to take deeper images to construct a sample of much fainter LAEs. We still have difficulties to make a meaningful comparison with the simulation, due to the shallowness of the data: the luminosity range of our observed samples corresponds to the very bright end of the mock LAEs. Constructing a sample of fainter LAEs ($\log(L_{\text{Ly}\alpha}) \lesssim 43$; $\lesssim 42.7$ when $h = 0.7$ is assumed), which is less likely to be contaminated by AGN, is essential to probe the LF and its environmental dependence. The uncertainty in the redshifts is also a problem in computing the galaxy density and the luminosities, as well as evaluating the contamination of AGN and foreground galaxies. Further deep imaging to construct a deeper sample, and subsequent

follow-up spectroscopy, are needed to draw further information from this comparison.

5 CONCLUSIONS

We have carried out intermediate-band and broadband imaging observations with Suprime-Cam on the Subaru Telescope of a $z = 4.1$ radio galaxy associated with a giant Ly α nebula to probe its environment on a $\sim 50 h^{-1}$ Mpc scale. In order to quantify the environment with a control sample, we utilized the existing data from a blank field, SXDS, taken with the same instrument and similar filters. We also used a mock LAE catalogue generated with a semi-analytical galaxy formation model based on the Millennium Simulation.

We confirmed that the radio galaxy lies in a region with peak LAE number density of $1 + \delta_{\text{LAE}} = 4.1 \pm 0.5$ at the radio galaxy position, even after taking account of the relatively large redshift range covered by the *IA624* filter. The average density over the Suprime-Cam FoV is almost the same as that of the blank field within 2.5 percent, showing that the density contrast in this field is very high. These results suggest that radio galaxies associated with Ly α nebulae emerge in extreme overdensity environments. Comparing these with the mock LAEs, we found that such high-density regions are quite rare, 25 peaks in the whole simulation volume of $(500 h^{-1} \text{Mpc})^3$, and correspond to the densest > 0.1 percentile. The corresponding number density is comparable to that of Coma-type protoclusters found in the same simulation, and known radio galaxies at $z > 2$. The overdensity associated with the radio galaxy can be traced up to $\sim 10 - 20 h^{-1}$ comoving Mpc, facing the large void region just adjacent to it. Only one of the 25 density peaks have such a large density contrast on this scale, and even this peak cannot fully reproduce the density peak profile.

We found the density dependence of the luminosity functions (LFs). The Ly α LF of the TNJ1338 field shows enhancement at the bright end ($\log(L_{\text{Ly}\alpha} [h^2 \text{erg s}^{-1}]) \gtrsim 43.6$) by an order of magnitude or more, while the faint end almost agrees with that in the blank field. We compared the LFs with the mock LAEs to conclude that star-formation and/or AGN activities affecting the bright end of the LF are highly enhanced within overdense regions. We pointed out the possibilities that frequent galaxy mergers or high gas-accretion rate enhance the star-formation / AGN activity, or AGN-induced star formation in this field. The presence of a powerful radio galaxy showing a giant Ly α nebula is thus a possible signpost of changes in galaxy formation activity on scales of $\sim 10 - 20 h^{-1}$ comoving Mpc.

ACKNOWLEDGEMENTS

We thank Masami Ouchi for providing the data of luminosity functions, and giving us useful comments. We thank Yi-Kuan Chiang, Surhud More and John Silverman for having discussion over this work, and giving us valuable comments. This work was supported by the FIRST programme “Subaru Measurements of Images and Redshifts (SuMIRe)”, World Premier International Research Center Initiative (WPI Initiative), MEXT, Japan. This work was supported in part by

the Science and Technology Facilities Council rolling grant ST/I001166/1 to the ICC. Calculations were partly performed on the ICC Cosmology Machine, which is part of the DiRAC Facility jointly funded by STFC and Durham University. YM acknowledges support from JSPS KAKENHI Grant Number 20647268. IRS acknowledges support from STFC (ST/I001573/1), the ERC Advanced Investigator programme DUSTYGAL 321334 and a Royal Society/Wolfson Merit Award. The data were in part obtained from SMOKA, which is operated by the Astronomy Data Center, National Astronomical Observatory of Japan.

REFERENCES

- Baba H. et al. 2002, ADASS XI eds. D. A. Bohlender, D. Durand, and T. H. Handley, ASP Conference series, 281, 298
- Basu-Zych A., Scharf C., 2004, *ApJ*, 615, L88
- Bertin E., Arnouts S., 1996, *A&AS*, 117, 303
- Blain A. W., Chapman S. C., Smail I., Ivison R., 2004, *ApJ*, 611, 725
- Bruzual G., Charlot S., 2003, *MNRAS*, 344, 1000
- Capak P. L., et al., 2011, *Nature*, 470, 233
- Chambers K. C., Miley G. K., van Breugel W. J. M., 1990, *ApJ*, 363, 21
- Chiang Y.-K., Overzier R., Gebhardt K., 2013, *ApJ*, 779, 127
- Cole S., Lacey C. G., Baugh C. M., Frenk C. S., 2000, *MNRAS*, 391, 168
- Croft S., Kurk J., van Breugel W., Stanford S. A., de Vries W., Pentericci L., Röttgering H., 2005, *AJ*, 130, 867
- Dawson S. et al., 2004, *ApJ*, 617, 707
- Dawson S., Rhoads J. E., Malhotra S., Stern D., Wang J.-X., Dey A., Spinrad H., Jannuzi B. T., 2008, *ApJ*, 671, 1227
- De Breuck C., van Breugel W., Minniti T., Miley G. K., Röttgering H. J. A., Stanford S. A., Carilli C., 1999, *A&A*, 352, L51
- De Breuck C., et al., 2001, *ApJ*, 121, 1241
- De Breuck C. et al., 2004, *A&A*, 424, 1
- Dekel A., et al., 2009, *Nature*, 457, 22
- Digby-North J. A., et al., 2010, *MNRAS*, 407, 853
- Dijkstra M., Haiman Z., Spaans M., 2006, *ApJ*, 649, 14
- Dijkstra M., Loeb A., 2009, *MNRAS*, 408, 1109
- Dijkstra M., Kramer R., 2012, *MNRAS*, 424, 1672
- Erb D. K., Bogosavljević M., Steidel C. C., 2011, *ApJ*, 740, L31
- Fardal M. A., Katz N., Gardner J. P., Hernquist L., Weinberg D. G., Davé R., 2001, *ApJ*, 562, 605
- Faucher-Giguère C.-A., Kereš D., Dijkstra M., Hernquist L., Zaldarriaga M., 2010, *ApJ*, 725, 633
- Fukugita M., Shimasaku K., Ichikawa T., 1995, *PASP*, 107, 945
- Furlanetto S. R., Schaye J., Springel V., Hernquist L., 2005, *ApJ*, 622, 7
- Furusawa H. et al., 2006, *ApJS*, 176, 1
- Geach J. E., Alexander D. M., Lehmer B. D., Smail I., Matsuda Y., Chapman S., Sharf C. A., Ivison R. J., Volonteri M., Yamada T., Blain A. W., Bower R. G., Bauer F. E., Basu-Zych A., 2009, *ApJ*, 700, 1
- Geach J. E., Matsuda Y., Smail I., Chapman S. C., Yamada T., Ivison R. J., Hayashino T., Ohta K., Shioya Y., Taniguchi Y., 2005, *MNRAS*, 363, 1398
- Goerdt T., Dekel A., Sternberg A., Ceverino D., Teyssier R., Primack J. R., 2010, *MNRAS*, 407, 613
- Hayashino T., et al., 2000, *Proc. SPIE*, 4008, 397
- Intema H. T., Venemans B. P., Kurk J. D., Ouchi M., Kodama T., Röttgering H. J. A., Miley G. K., Overzier R. A., 2006, *A&A*, 456, 433
- Ivison R. J., et al., 2013, *ApJ*, 772, 137
- Iye M., et al., 2004, *PASJ*, 56, 381
- Kennicutt R. C., 1983, *MNRAS*, 301, 569
- Ker L. M., Best P. N., Rigby E. E., Röttgering H. J. A., Gendre M. A., 2012, *MNRAS*, 420, 2644
- Kereš D., Katz N., Weinberg D. H., Davé R., 2005, *MNRAS*, 363, 2
- Kovač K., Somerville R. S., Rhoads J. E., Malhotra S., Wang J.-X., 2007, *ApJ*, 668, 15
- Koyama Y., et al., 2013, *MNRAS*, 434, 423
- Le Delliou M., Lacey C., Baugh C. M., Guiderdoni B., Bacon R., Courtois H., Sousbie T., Morris S. L., 2005, *MNRAS*, 357, L11
- Le Delliou M., Lacey C., Baugh C. M., Morris S. L., 2006, *MNRAS*, 365, L712
- Lehmer B. D., et al., 2009, *MNRAS*, 400, 299
- Madau P., 1995, *ApJ*, 441, 18
- Massey P., Strobel K., Barnes J. V., Anderson E., 1988, *ApJ*, 328, 315
- Matsuda Y., Yamada T., Hayashino T., Yamauchi R., Nakamura Y., 2006, *ApJ*, 640, L123
- Matsuda Y., et al., 2011, *MNRAS*, 410, L13
- Matsuda Y., et al., 2012, *MNRAS*, 425, 878
- Miley G., et al., 2004, *Nature*, 427, 47
- Miley G. & De Breuck, 2008, *ARAA*, 15, 67
- Miyazaki S., et al., 2002, *PASJ*, 54, 833
- Mori M., Umemura M., 2006, *Nature*, 440, 644
- Nelson, D., Vogelsberger, M., Genel, S., et al. 2013, *MNRAS*, 429, 3353
- Nilsson K. K., Fynbo J. P. U., Møller P., Sommer-Larsen J., Ledoux C., 2006, *A&A*, 452, L23
- Ohya Y., et al., 2003, *ApJ*, 591, L9
- Oke J. B., 1974, *ApJS*, 27, 21
- Orsi A., Lacey C., Baugh C. M., Infante L., 2008, *MNRAS*, 391, 1589
- Ouchi M., et al., 2004, *ApJ*, 611, 660
- Ouchi M., et al., 2005, *ApJ*, 620, L1
- Ouchi M., et al., 2008, *ApJS*, 176, 301
- Ouchi M., et al., 2010, *ApJ*, 723, 869
- Overzier R. A., et al. 2008, *ApJ*, 673, 143
- Pentericci L., Kurk J. D., Carilli C. L., Harris D. E., Miley G. K., Röttgering H. J. A., 2002, *A&A*, 396, 109
- Moorwood A. F. M., Adelberger K. L., Giavalisco M., 2001, *ApJ*, 554, 981
- Rees M. J., Ostriker J. P., 1977, *MNRAS*, 179, 541
- Reuland M., et al., 2003, *ApJ*, 592, 755
- Rhoads J. E., Malhotra S., Dey A., Stern D., Spinrad H., Jannuzi B. T., 2000, *ApJ*, 545, L85
- Röttgering H. J. A., Hunstead R., Miley G. K., van Ojik R., Wieringa M. H., 1995, *MNRAS*, 277, 389
- Saito T., Shimasaku K., Okamura S., Ouchi M., Akiyama M., Yoshida M., 2006, *ApJ*, 648, 54

- Saito T., Shimasaku K., Okamura S., Ouchi M., Akiyama M., Yoshida M., Ueda Y., 2008, *ApJ*, 675, 1076
- Schlegel D. J., Finkbeiner D. P., Davis M., 1998, *ApJ*, 500, 525
- Smail I., Blundell M., 2013, *MNRAS*, 434, 3246
- Smith D. J. B., Jarvis M. J., 2007, *MNRAS*, 378, L49
- Springel V. et al., 2005, *Nature*, 435, 2
- Stone R. P. S., 1996, *ApJS*, 107, 423
- Steidel C. C., Adelberger K. L., Shapley A. E., Erb D. K., Reddy N. A., Pettini M., 2005, *ApJ*, 626, 44
- Steidel C. C., Erb D. K., Shapley A. E., Pettini M., Reddy N., Bogosalić M., Rudie G. C., Rakic O., 2010, *ApJ*, 717, 289
- Taniguchi Y., 2004, *Proc. Japan-German Seminar, Sendai 2001* (Eds: Arimoto N. and Duschi W.), 107
- Taniguchi Y., Shioya Y., 2000, *ApJ*, L13
- Tenorio-Tagle G., Silich S. A., Kunth D., Terlevich E., Terlevich R., 1999, *MNRAS*, 309, 332
- Uchimoto Y. K., et al., 2008, *PASJ*, 60, 683
- Uchimoto Y. K., et al., 2012, *ApJ*, 750, 116
- van Ojik R., Röttgering H. J. A., Carilli C., Bremer M. N., Macchetto F. A., 1996, *A&A*, 313, 25
- van Ojik R., Röttgering H. J. A., Miley G. K., Hunstead R. W., 1997, *A&A*, 317, 358
- Veilleux S., Cecil G. Bland-Hawthorn J., 2005, *ARAA*, 43, 769
- Venemans B., et al., 2002, *ApJ*, 569, L11
- Venemans B., et al., 2007, *A&A*, 461, 823
- Villar-Martin M., Sánchez S. F., Humphrey A., Dijkstra M., di Serego Alighieri S., De Breuck C., Gonzalez Delgado R., 2007, *MNRAS*, 378, 416
- Wilman R. J., Gerssen J., Bower R. G., Morris S. L., Bacon R., de Zeeuw P. T., Davies R. L., 2005, *Nature*, 436, 227
- Yagi M., Kashikawa N., Sekiguchi M., Doi M., Yasuda N., Shimasaku K., Okamura S., 2002, *AJ*, 123, 66
- Zirm A. W., et al., 2005, *ApJ*, 630, 68

APPENDIX A: THREE-DIMENSIONAL DENSITY PROFILES

As discussed in the §4.3.2, such a high density peak and a large void region within a single FoV as we found in the TNJ1338 field is likely to be reproduced by fields with large G 's, like the G478 field. However, although the G478 field has very large G , the peak density is only ~ 3.2 when normalised within the field, since the G478 field has large plateau of the density. Unlike the G478 field, the three fields shown here have relatively steep peaks on their centres. They also have relatively large G 's: two of these are the fields with the second- and third largest G . The G 's for these three fields are 0.371, 0.349, and 0.307 for Peak 1, 13, and 21, respectively. This kind of differences becomes clearer when we look into the three-dimensional (3-D) densities. We calculated the local- and global densities using the 3-D spatial distribution of the mock LAEs within these fields. The density at the position of each source was calculated based on the distance to the 5th-, 10th- and 20th-nearest neighbour. We normalised the density with the average over the same field, and calculated the overdensity $\delta_{5\text{th}}$, $\delta_{10\text{th}}$, and $\delta_{20\text{th}}$. Then we counted the LAEs residing in the density greater than the average.

Table A1 summarizes the results of the density measurements of these four high-density fields, comparing with the observed data.

Among the four high-density fields shown here, the G478 field has the largest fraction of LAEs lying within the overdensities in terms of $\delta_{5\text{th}}$ and $\delta_{10\text{th}}$. However, this field does not have regions of $\delta_{20\text{th}} > 0$. On the other hand, the Peak 21 field does not have such a high fraction of $\delta_{5\text{th}} > 0$ and $\delta_{10\text{th}}$, but has three sources lying within $\delta_{20\text{th}} > 0$ regions. The remaining two fields, Peak 1 and 13, show the clustering signals which are in between the G478 and the Peak 21 fields. The average 3-D density corresponds to the distance of the 5th-, 10th- and 20th-nearest neighbour of 8.5, 12 and 19 h^{-1} comoving Mpc, respectively. Comparing the two fields, the overdensities spread more widely in the G478 field than in the Peak 21 field. The high-density regions are concentrated along the line of sight at $340 \lesssim z \lesssim 390 h^{-1}$ Mpc in the Peak 21, and seems to spread more widely over the sky than in the G478 field (Fig. A1).

The high surface-density peak seen at the centre of G478 field is thus likely to be clumps of LAEs forming a filamentary structure elongated toward the line of sight, rather than a single extremely overdense region. If radio galaxies are formed within extremely overdense regions, the Peak 21 is more likely to be reproducing the environment of radio galaxies. However, as expected from the relatively small G 's compared with the TNJ1338 field, the Peak 21 field do not have such a large fraction of void regions as seen in the TNJ1338 or G478 fields. The Peak 21 seems to be rather evolved protocluster, in which LAEs are clustered up to a few tens of comoving Mpc, but such evolved protocluster cannot reproduce the large fraction of void regions. Similarly, overdense regions containing very massive dark haloes (the maximum halo mass in the simulation, $9.4 \times 10^{12} M_{\odot}$) do not reproduce the high peak density and the large density contrast. One of the 25 peaks described above contains such a massive dark halo, but the field around this peak have the peak density only up to $1 + \delta_{\text{LAE}} = 2.90$ when normalised within the same field, and have relatively small void fraction leading to $G = 0.289$.

These analyses together suggest that the simulation cannot fully reproduce the density distribution of the TNJ1338 field. The environment of this field is thus extremely rare, more than an order of magnitude lower density than known radio galaxies at $z > 2$.

Table A1. Density measurements around the high-density peaks

Field	N_{tot}^a	$\max(1 + \delta_{\text{LAE}})^b$	$N(\delta_{\text{LAE}} > 0)^c$	$N(\delta_{5\text{th}} > 0)^d$	$N(\delta_{10\text{th}} > 0)^d$	$N(\delta_{20\text{th}} > 0)^d$
G478	72	3.2	51	22	13	0
Peak 1	84	3.5	56	13	3	0
Peak 13	79	3.5	43	3	0	0
Peak 21	83	3.5	42	13	8	3
TN J1338-1942	31	4.1	27	-	-	-
(SXDS) ^e	34	2.4	29	-	-	-

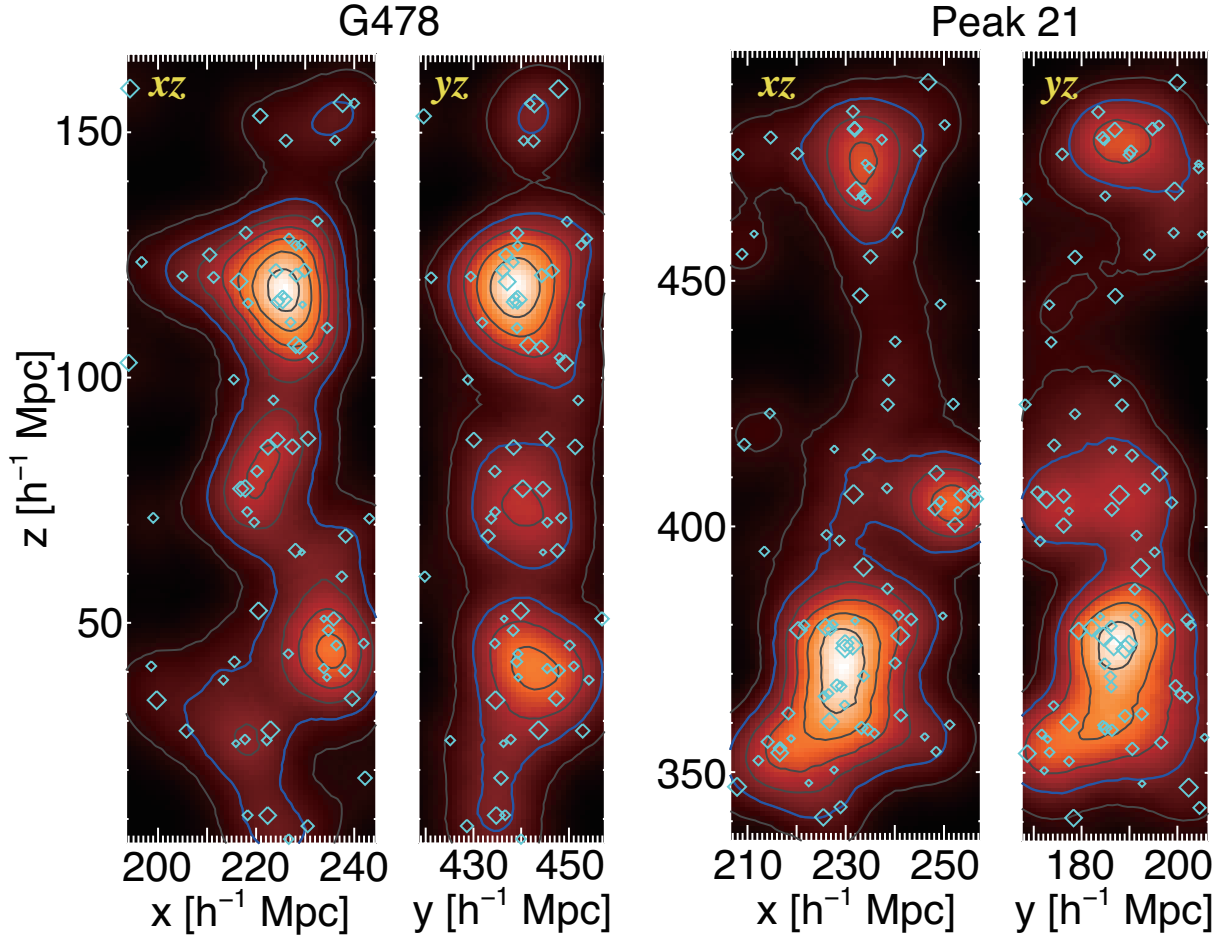
^aTotal number of LAEs within the field.^bThe peak (maximum) surface density within the field.^cThe number of LAEs with the surface density greater than the average.^dThe number of LAEs with the 3-D densities greater than the average. The densities were calculated from the 5th-, 10th- and 20th-nearest neighbours for $\delta_{5\text{th}}$, δ_{rm10th} and δ_{20th} , respectively.^eControl field (not a high-density peak).

Figure A1. LAE density maps of the two fields with high-density peaks, generated with the mock LAEs projected onto the xz - and yz planes, instead of the xy plane shown in Fig. 4. The left two panels are the maps for the G478 field, projected on the xz - (left) and the yz plane (right). The right two panels are for the Peak 21 field. The overdense region in the G478 field emerged on the xy -plane density map seems to have sub-clumps that are distributed over a wide range along the z axis. On the other hand, the density distribution in the Peak 21 is relatively concentrated at $z \sim 340 - 390 h^{-1}\text{Mpc}$, except for the minor clump at $z \sim 480$. All the coordinates shown here are in the comoving scales. The maps are drawn with the same manner as in Fig. 4, except for the use of smoothing radius of $8 h^{-1}\text{Mpc}$.